Applied Catalysis B: Environment and Energy 385 (2026) 126276

Contents lists available at ScienceDirect

Applied Catalysis B: Environment and Energy

journal homepage: www.elsevier.com/locate/apcatb

# Streamlining $CO_2$ photoelectrocatalytic conversion to $C_{2+}$ products using CuMg-based LDH: A single-material photocathode strategy

Eleonora Tosi Brandi [a,d], Jacopo De Maron [a,d], Andrea Fasolini [a,d], Nicola Sangiorgi [b], Alex Sangiorgi [b], Marco Etzi [c,e], Erika Scavetta [a,d], Alessandra Sanson [b,**], Francesco Basile [a,d,e,*]

[a] Department of Industrial Chemistry "Toso Montanari", University of Bologna, Via Gobetti 85, Bologna 40129, Italy
[b] National Research Council of Italy, Institute of Science, Technology and Sustainability for Ceramics (CNR-ISSMC), Via Granarolo 64, Faenza 48018, Italy
[c] Center for Sustainable Future Technologies, Istituto Italiano di Tecnologia, Via Livorno 60, Torino 10144, Italy
[d] Center for Chemical Catalysis - C3, University of Bologna, Via Gobetti 85, Bologna 40136, Italy
[e] Consorzio Interuniversitario per La Scienza e Tecnologia Dei Materiali (INSTM), Via G. Giusti, 9, Florence 50121, Italy

ARTICLE INFO

*Keywords:*
Photoelectrochemical $CO_2$ conversion (PEC)
Layered Double Hydroxides (LDH)
CuMgAl hydroxide
CuMgFe hydroxide
Solar fuels

ABSTRACT

The photoelectrocatalytic reduction of $CO_2$ to valuable products using renewable energy is a promising approach to address decarbonization. PEC systems rely on photocathodes composed of a photoactive phase and a catalytically active one. The integration of such heterogeneous surfaces is difficult to achieve. Herein, we propose for the first time the use of Cu-containing Layered Double Hydroxide as single-phase photocathode material for light-assisted $CO_2$ conversion providing simultaneous light-absorption and $CO_2$ electroreduction. Exploiting the variability in composition and $CO_2$ affinity of LDHs $CO_2$ conversion into $C_2$ and $C_3$ oxygenates have been performed in a PEC system under low applied voltage. Taking advantage of reproducible and scalable procedures single-phase materials for photoelectrodes (Cu/Mg/Al and Cu/Mg/Fe) were obtained. Characterization of structure/morphology, photoelectrochemical, and catalytic properties allowed deep understanding of the role of metal elements within LDH structure on photocathodes performances. Iron provided strong benefits to light-harvesting and electrocatalytic activity.

## 1. Introduction

In the quest for sustainable energy and effective carbon management strategies, the utilization of renewable resources for the reduction of carbon dioxide emissions has emerged as a critical area of research. Since the adoption of the Paris Agreement and the release of the IPCC Special Report on Global Warming of 1.5 °C, a growing number of countries have committed to net zero emissions targets. As of March 2022, 33 countries and the European Union have set such a target, either in law or in a policy document. More than 100 countries have proposed - or are considering - a net zero target [1]. Among the myriads of approaches, photoelectrochemical $CO_2$ reduction reaction ($CO_2$RR) has garnered significant attention for its potential to harness solar energy to drive the conversion of $CO_2$ into valuable fuels and chemicals. This transformative process holds promise not only for mitigating the escalating levels of atmospheric $CO_2$ but also for producing renewable fuels that could help meet the world's growing energy demands.

The escalating global concerns surrounding climate change and the depletion of conventional energy sources necessitate the exploration of innovative technologies that can address these challenges concurrently. The conversion of $CO_2$ into valuable products at ambient temperature can be pursued via a process involving the reduction of carbon dioxide by photo-generated electrons through a photoelectrocatalyst. To do so, the development of semiconductor materials able to both absorb light and conduct/transfer electrons is necessary [2–4].

Photoelectrochemical (PEC) $CO_2$ conversion with tailored photoelectrocatalysts is a promising technology with its own set of advantages and challenges. Indeed, this approach could allow renewable energy utilization, direct $CO_2$ conversion to various products, integration with renewable energy systems, but it suffers from several drawbacks and technological limitations such as material stability, overall system efficiency, product selectivity, costs, scaling up [5,6].

* Corresponding author at: Department of Industrial Chemistry "Toso Montanari", University of Bologna, Via Gobetti 85, Bologna 40129, Italy.
** Corresponding author.
*E-mail addresses:* alessandra.sanson@issmc.cnr.it (A. Sanson), f.basile@unibo.it (F. Basile).

https://doi.org/10.1016/j.apcatb.2025.126276
Received 16 October 2025; Received in revised form 30 November 2025; Accepted 2 December 2025
Available online 5 December 2025

An efficient PEC system requires (i) a photo-absorber with suitable band gap and band energy to absorb solar energy in a certain range of light spectrum and to produce photo-induced electrons and holes with useful redox potentials; (ii) a catalyst to accelerate the reaction kinetics, improve reaction selectivity, and enhance charge-carrier transport at the surface. Semiconductors, including transition metal oxides, Si, III–V and II–VI photo-absorbers, perovskite materials, carbon nitrides, metal–organic frameworks and metal complexes are well-studied materials generally employed as photo-absorbers in PEC systems [7]. Besides, the possibility to exploit the photo-absorbing phase also as catalyst would reduce the complexity in efficient photoelectrodes production and might also increase the output of the chemical transformation process. In this context, it is well-established that Cu is the only transition metal element able to promote C-C coupling of $CO_2$ species adsorbed on catalysts surface [8,9]. For this reason Cu-based photocathodes have attracted wide attention, and in literature many studies can be found involving pure copper oxides (CuO, $Cu_2O$) [10–13], binary and ternary oxides and sulphides, chalcogenides, and Cu-based composites [14–16].

Noteworthy, Cu/Fe binary oxides have been studied as photocathodes for $CO_2$ photoelectrochemical reduction and tuned out to be effective for carbon dioxide conversion into methanol [17,18], formate [19], and acetate [20].

Layered double hydroxides (LDHs) are another interesting class of advanced and versatile materials that can be exploited to produce copper-based photoelectrocatalysts. Indeed, this category of compounds may hold significant promise for $CO_2$RR applications thanks to their alkaline nature and strong affinity for carbonates. Often referred to as hydrotalcite-like compounds, layered double hydroxides are a type of anionic clays with formula $[M(II)_{1-x}M(III)_x(OH)_2]^{x+}\left(A^{n-}_{x/n}\right)\bullet mH_2O$. These compounds are made up of layers in which the cations are coordinated octahedrally by $OH^-$ to form layered structures, and anions are intercalated between the layers to maintain their overall positive charge resulting from the partial substitution of M(II) with M(III) [21]. The ease in hosting different metal cations and their ability to exchange the interlayer anions contribute to the appeal of LDHs for use in various applications as catalysts [22–28], electrochemical sensors [29–33], drugs and biologically active compounds carriers [34,35], absorbers of contaminant [36–38], and additives [39,40]. With regards to their applications in catalysis, LDH-derived materials are primarily recognized as catalyst precursors for methane reforming into syngas, for the hydrogenation of $CO_2$ to methane or methanol [41–50], and for other thermocatalytic applications [51]. However, recently a great interest in these materials has risen in the field of photocatalysis and electrocatalysis. In fact, the possibility of tuning the redox properties and the light absorption capacity by playing with metal cations composition as well as with functional anion intercalation, led to the application of this class of compound as electrocatalysts for water splitting, especially for oxygen evolution reaction [52–54], organic substrates electrooxidation [55–58], and $CO_2$ electrochemical reduction [59–62]. In the field of photocatalysis, LDHs found large employment as photocatalysts in water splitting [63–65] and $CO_2$ conversion [66–69]. Meanwhile LDH-based photoelectrodes are studied for PEC water splitting [70–75] but also for energy production in Dye-Sensitized Solar Cells [76–78].

Despite this, studies on single-phase LDH-based photocathodes for the $CO_2$ reduction reaction ($CO_2$RR) are scarce, particularly those that exploit their dual function as both a light absorber and a catalyst. [79,80].

In this work, we propose the use of two trimetallic LDH materials (i.e., Cu/Mg/Al and Cu/Mg/Fe LDHs) synthesized with the same molar ratios between Cu/Mg and M(II)/M(III) as photocathodes for $CO_2$RR in PEC systems. While Al as trivalent metal cation has already been proven selective for acetic acid production in previous $CO_2$ reduction experiments [62], the Fe insertion in the LDH structure aims to enhance conductivity and visible-light absorption thanks to its sensitizing effect [77,81] for light-assisted $CO_2$ electrolysis. LDHs were prepared by coprecipitation and photocathodes were manufactured by screen printing, with both methods being reliable and scalable. The morphology, structure, and chemical composition of both powder and film samples were fully investigated by means of several complementary techniques, proving the photocathodes underwent phase activation under reaction conditions providing catalytically active $Cu^0/Cu_2O$ species over light-absorbing and carbonates-concentrating LDH phase. The photoelectrocatalytic properties of the materials were studied during light-assisted potentiostatic $CO_2$RR in liquid phase ($KHCO_3$) by evaluating the effect of the trivalent cation species on the resulting catalytic performances. This study demonstrates the beneficial effects of using layered double hydroxide structure with highly dispersed copper species, which allows to obtain (i) a $C_2$ and even $C_3$ product at a low potential applied during $CO_2$RR.

## 2. Experimental

### 2.1. Materials synthesis

Ternary layered double hydroxides powders, named CuMgAl-LDH and CuMgFe-LDH, were prepared by a coprecipitation method. In detail, 2 M aqueous solutions of metallic cations were prepared from metal nitrates salts: $Cu(NO_3)_2\bullet 2.5\ H_2O$ (98 %, Sigma-Aldrich), $Mg(NO_3)_2\bullet 6\ H_2O$ (99 %, Sigma-Aldrich), $Al(NO_3)_3\bullet 9\ H_2O$ (98 %, Sigma-Aldrich), $Fe(NO_3)_3\bullet 9\ H_2O$ (98 %, Sigma-Aldrich). The amount of each cation in the solution was calculated according to a relative molar ratio of Cu: Mg: Al or Fe = 2:1: 1.

The cations' solution was then added dropwise to a 1 M $Na_2CO_3$ solution keeping the pH constant at the value of 9 by adding 3 M NaOH. During the synthesis the solution was kept under stirring at the constant temperature of 56°C.

After the complete addition of the cations' solution to the anion solution, the synthesis mixture was left under the same conditions of coprecipitation for an hour to allow the ageing process.

Afterwards, the obtained precipitate was filtered with a Buchner funnel and fully washed with DI water until a neutral pH of filtration water was reached. The solid was collected and dried in oven at 60°C overnight.

### 2.2. Photoelectrodes preparation

Screen-printing inks containing CuMgAl and CuMgFe LDH compounds were formulated and prepared by mixing the respective powders with organic additives:

α-terpineol (Sigma- Aldrich) as solvent, lauric acid as dispersant (Merck, Germany), ethyl cellulose as binder (Sigma-Aldrich), and finally glycerol (Merck, Germany) as plasticizer. The powders were firstly dispersed in the solvent and the different organics were added to obtain a stable suspension and the suitable rheology for the selected deposition process. The as-formulated inks were finally homogenized in a three-roll mill equipped with $ZrO_2$ rollers (Exakt 80E, Exakt, Nordestedt, Germany) and then, deposited onto Fluorine-doped Tin Oxide (FTO) glass substrates (sheet resistance 7 Ω/sq., Sigma-Aldrich) using a semi-automatic screen-printer (AUR'EL 900, AUR'EL Automation s.p.a., Italy) [78] to obtain films having area equal to 1 $cm^2$ and a catalyst's loading of about 0.7 mg $cm^{-2}$. The latter were subsequently dried by an IR thermal treatment performed at 180 °C for 3 h to avoid the LDH degradation. The film thickness was fixed in the 6–7 μm range, as confirmed by profilometry.

### 2.3. Structural and morphological characterization

X-ray diffraction (XRD) analyses were carried out with a Philips PW1050/81 diffractometer equipped with a graphite monochromator in the diffracted beam and controlled by a PW1710 unit (Cu Kα, λ =0.15418 nm). A 2θ range from 5° to 80° was investigated at a speed of

0.05°/s. Crystallites' mean size was calculated according to the Scherrer equation (Eq.1):

$$D_{hkl} = K\frac{\lambda}{\beta cos\theta} \quad (1)$$

Where $D_{hkl}$ is the mean crystallite dimension, $K$, equal to 0.9, is a dimensionless shape factor, $\lambda$ is the X-ray wavelength (Cu Kα), $\beta$ is the line broadening at half the maximum intensity (FWHM) of the reflex after correction for the instrumental line broadening, $\vartheta$ is the Bragg angle of the considered reflex.

The specific surface area (SSA) of LDHs has been measured by means of single point $N_2$ physisorption with the BET method using a SORPTY 1750 instrument (Fisons); usually the analysis was carried out over about 0.1 g of sample.

Scanning Electron Microscopy (SEM) has been carried out to acquire morphological and surface information on both the LDHs powders and films deposited on the conductive support. The analyses were performed through a Zeiss ΣIGMA SEM-FEG.

TEM analyses were conducted using a TALOS F200X (Thermo Fischer Scientific), operated at a tension of 200 kV. Plasma cleaning was eventually conducted on the samples before the analysis with a plasma cleaner Femto model (Diener GmbH).

Raman spectra were recorded with a micro-spectrometer Raman RM1000 (Renishaw/Thermo Fisher, New Mills, Wotton-under-Edge, Gloucestershire, UK) equipped with a Leica DMLM optical microscope and a CCD detector. The excitation wavelength came from an $Ar^+$ laser (λ = 514.5 nm) with an output power of 25 mW. This power was reduced as needed by neutral density filters for preventing sample damage.

Profilometric analysis have been carried out on films deposited on the FTO by a white light-optic interferometer BRUKER CounterGT-K 3D.

X-ray Photoelectron Spectroscopy (XPS) measurements were conducted on a PHI 5000 Versaprobe spectrometer equipped with a monochromatic Al Kα (1486.6 eV) X-ray source. An electron gun and an Ar ion gun were used as a charge compensation system. The spot size was 100 μm. The pass energy was set at 187.85 eV and 23.5 eV for the acquisition of survey and high-resolution spectra, respectively. Binding energy calibration was applied by setting the position of the C 1 s $sp^3$ component at 284.8 eV. The spectra were processed using CasaXPS software (v2.3.23, Casa Software Ltd).

### 2.4. Photoelectrochemical measurements

Spectrophotometric determination of the film bandgap (Eg) was performed using the absorption spectra recorded in transmission mode using a PVE300 system (Bentham Instruments Ltd, United Kingdom) and applying the Tauc equation (Eq. 2):

$$\alpha h\nu = A(h\nu - E_g)^n \quad (2)$$

where α is the absorption coefficient, h is the Planck's constant [J•s], $\nu$ is the light frequency ($s^{-1}$), A is the absorption constant, and $E_g$ is the value of the bandgap energy (eV), whereas the exponential n refers to the type of electronic transition specific to the semiconductor [82]. For this type of materials the use of n = 2, indicating a direct electronic transition, is widely agreed in literature and therefore used here for the calculation of the band gap by Tauc equation [63,83,84].

All electrochemical measurements were performed with a Autolab PGSTAT302N+FRA32M (Metrohm) potentiostat/galvanostat.

Potentials are hereby converted versus RHE using Eq. 3 to allow the comparison with previous work and literature, with $E^0_{Ag/AgCl}$ and pH equal to 0.197 and 7.15 ($KHCO_3$ 0.3 M) or 13 (KOH 0.1 M), respectively.

$$E_{RHE} = E_{Ag/AgCl} + E^0_{Ag/AgCl} + 0.059 \bullet pH \quad (3)$$

Electrochemical impedance spectroscopy (EIS) measurements have been carried out in 0.3 M $KHCO_3$ electrolyte saturated with $CO_2$, Ag/AgCl and Pt gauze as reference and counter electrodes, respectively. Two distinct potentials were applied, i.e. OCP (determined for each electrode in dark condition before EIS measurements) and – 0.4 V vs RHE, with an amplitude of ± 10 mV, in a frequency range of $10^5$ – 0.5 Hz.

The Mott-Schottky analysis has been carried in a three-electrode cell in which the film represents the working electrode, a saturated standard calomel electrode (SCE) is used as reference, and a platinum wire is the counter electrode. The electrolyte used was a 0.1 M $Na_2SO_4$ solution, and the potential range used was + 0.6 V/-0.6 V vs SCE, with EIS analyses in a frequency range of $10^5$-0.5 Hz and signal amplitude of ± 10 mV [85]. The Mott−Schottky equation (Eq. 4) is as follows:

$$\frac{1}{C^2} = \frac{2}{\varepsilon \bullet \varepsilon_0 \bullet A^2 \bullet e \bullet N_D} \bullet \left( -V + V_{fb} - \frac{k_B \bullet T}{e} \right) \quad (4)$$

where C is the interfacial capacitance, A is the interfacial area, $N_A$ the number of acceptors, V is the applied voltage, $k_B$ is Boltzmann's constant, T the absolute temperature, and $e$ is the electronic charge; a linear plot of $C^{-2}$ vs V yields the flat band potential, calculated by adding the $k_BT/e$ term from the intersection point on the ordinate [86]. The calculated flat band potentials for both samples were then referred vs. the Normal Hydrogen Electrode (NHE) at pH = 7 by means of Eqs. 5 – 6.

$$V_{fb\ (pH=0)} = V_{fb\ (pH=n)} - 0.059 \times (0 - n) \quad (5)$$

$$V_{fb}\ (vs.\ NHE) - V_{fb}\ (vs.\ SCE) = 0.244\ V \quad (6)$$

The photo-electrochemical activity has been evaluated by linear sweep voltammetry (LSV) with and without the presence of light. As electrochemical setup a single compartment PEC was used in which the prepared photocathodes represent the working electrode, an Ag/AgCl electrode is used as reference, and a platinum wire is the counter electrode. Light conditions have been created through a solar simulator calibrated with a silicon cell to obtain an overall power of 1000 W/$m^2$ AM 1.5. The potential range used was 0.7 V/-0.5 V vs RHE, applying a scan rate of 0.01 V/s and KOH 0.1 M was used as electrolyte. The solution was degassed with argon for 15 min prior to the measurement to remove the oxygen dissolved from the solution. Transient photocurrent was measured by chronoamperometry at 0 V vs RHE in $KHCO_3$ aqueous electrolyte performing light chopping with a frequency of 0.2 Hz The determination of the electrochemical active surface area (ECSA) was carried out varying the scan rate of different cyclic voltammetries (1, 5, 10, 25, 50, 100 mV $s^{-1}$) recorded at 0.4 V vs Ag/AgCl (± 10 mV), which is a potential at which the photoelectrocatalysts displayed a capacitive current. The CVs were carried out in 1 M NaOH and the ECSA was calculated dividing the double-layer electrochemical capacitance ($C_{dl}$) by the specific capacitance of the sample (0.040 mF $cm^{-2}$ for flat metal surfaces in alkaline electrolyte) [87]. All the ECSA values are reported with the standard error (STD error = $\sigma/\sqrt{N}$).

For charge lifetime and capacitance determination, Electrochemical impedance spectroscopy (EIS) measurements in the dark have been carried out in 0.3 M $KHCO_3$ electrolyte saturated with $CO_2$, using Ag/AgCl and Pt gauze as reference and counter electrodes, respectively. Different potentials were applied equal to −0.8 V, −0.4 V and −0.2 V vs RHE with an amplitude of ± 10 mV, in a frequency range of $10^5$ – 0.5 Hz. EIS data were fitted using an equivalent circuit where Rs represents the contact series resistance, the electrolyte-photoanode interface is modelled by the built-in extended element which allows for transmission line impedance and the parallel $R_{CT}$//CPE stands for the electrolyte-electrode interface. Moreover, the charge lifetime was calculated following this equation [88,89]:

$$\tau_n = (R_{CT} \times Q_{\mu}\ )^{1/\beta}$$

where $R_{CT}$ represents the charge transfer resistance, and Qμ and β are the base and exponent of CPE element. Finally, the chemical capacitance of each photoelectrodes was determined using these CPE parameters.

The Incident photon-to current conversion efficiency (IPCE, or

external quantum efficiency) for CuMg-based LDH was determined using Autolab PGSTAT302N in combination with the Autolab Optical Bench, which is comprised of LED driver, different LED lights and optical rail. For that, 6 types of LED light sources were used with different wavelengths: 470 nm, 505 nm, 530 nm, 590 nm, 617 nm and 627 nm. These light sources were a triple Led array driven by the output current of the Autolab LED driver, and a calibrated light intensity of 1 mW $cm^{-2}$ was set. The output of the LED drive was controlled by the DAC164 of the Autolab directly from the Nova software. The obtained photocurrents in short circuit condition were acquired at each different wavelength by chronoamperometric method. A photo-electrochemical cell was used for this purpose, where a CuMg-based LDH was the working electrode, Ag/AgCl was the reference electrode and platinum gauze the counter-electrode. An electrolyte of $KHCO_3$ 0.3 M saturated with $CO_2$ was used. The quantum efficiency is defined as the ratio between the number of electrons generated and the photon flux on the photoactive surface area of the sample at a defined wavelength:

$$\mathrm{IPCE}(\%) = \frac{1239}{\lambda} \times \frac{J_{SC,\lambda}}{A \times P_I} \times 100$$

where $J_{SC,\lambda}$ is the photocurrent at a particular wavelength, λ is the wavelength, A (in $cm^2$) is the photoelectrode area and $P_i$ is the light intensity (mW $cm^{-2}$) [90].

### 2.5. Photoelectrocatalytic tests

The catalytic performances of LDH-based photocathodes were assessed in a single compartment PEC cell using a 0.3 M $KHCO_3$ solution (pH 8.50) as supporting electrolyte, saturated with $CO_2$, purged with a 0.3 L/min flux at a pressure of 1.5 bar for 15 min (pH 7.15), before carrying out carbon dioxide reduction tests. The working electrode, represented by the LDH-based film deposited on FTO, was connected to a Pt gauze, i.e. the counter electrode, while Ag/AgCl was used as reference electrode. An external bias was supplied by chronoamperometry technique through an Autolab PGSTAT302N+FRA32M (Metrohm) potentiostat/galvanostat. The analysis has been performed irradiating the photocathode from the FTO side. During the reaction, the solution has been maintained under stirring, while light conditions have been created through a solar simulator calibrated with a silicon cell to obtain an overall power of 1000 W/$m^2$ AM 1.5.

The $CO_2$RR reactions have been carried out for 1 h, analysing every 10 min the gas phase using a 990 micro-GC (Agilent Technologies) equipped with three channels (Molecular sieve 5 Å packed column for $H_2$, CO, $CH_4$ detection, PPU and 5CB columns for $CO_2$ and alkanes, alkenes respectively) and a thermal conductivity detector (TCD). Argon and helium were used as carrier gas. The liquid phase was analysed by a quantitative $^1$H NMR analysis, adding phenol as the internal standard and deuterium oxide to provide an internal lock signal.

## 3. Results

### 3.1. Structural and morphological characterization of materials

The as-synthesized Cu/Mg/Al and Cu/Mg/Fe LDHs obtained by coprecipitation method have been structurally characterized by X-Ray diffraction analysis before the formulation of the ink. XRD patterns reported in Fig. 1A evidenced the presence of a layered double hydroxide structure that shows the main reflections typical of the hydrotalcite-like structure [21,51,91] containing $CO_3^{2-}$ as interlayer anion, at 11.5°(003), 23.3°(006), 34.4°(012), 39.1°(015), 46.5°(018), 60.0°(110), 61.3°(113), and 65.2°(116) 2θ values for CuMgAl-LDH and 11.6°(003), 23.3°(006), 34.1°(012), 38.7°(015), 46.1°(018), 59.2°(110), 60.6°(113) 2θ values for CuMgFe-LDH. The Bragg angle of reflection 003 and 110 was used to calculate both the vertical and the horizontal dimension of the crystallites using the Scherrer equation (Eq.1, par. 2.3). Moreover, unit cell parameters were calculated from *d*-spacings of 003 and 110 reflections, which in turn were determined from Bragg law, as follows: $a = 2d_{110}$ and $c = 3d_{003}$ [92]. All structural data are reported Table 1. The two LDH samples resulted in very close crystallites' size and unit cell parameters. Crystallites height estimated for CuMgAl-LDH and CuMgFe-LDH was 10.3 and 9.8 nm, respectively, while the horizontal length resulted to be 13.7 and 16.1. Whilst *a* and *c* cell parameters resulted 3.08 and 23.0 Å for Al-containing LDH whereas 3.12 and 22.9 Å figured for Fe-containing LDH structure. The only remarkable difference is related to the shifting of 110, 113 and 116 reflections toward lower 2θ, indicating a larger D-spacing for CuMgFe-LDH with respect to CuMgAl-LDH, due to the larger ionic radius of $Fe^{3+}$ than that of $Al^{3+}$ [93]. The XRD analyses were also conducted after the deposition of the LDH-containing film on FTO (Fig. 1B) and allowed to confirm the retainment of layered double hydroxides phase of the material after ink formulation and film deposition onto FTO substrate. Moreover, 2θ angles, correspondent to 003 lattice planes, slightly shifted toward higher

**Table 1**
Calculated crystallite dimensions and specific surface area for CuMgAl-LDH and CuMgFe-LDH samples.

| *Sample* | *D-spacing (003) [Å]* | *D-spacing (110) [Å]* | $D_{003}$ *[nm]* | $D_{110}$ *[nm]* | *a [Å]* | *c [Å]* | *SSA [$m^2$/g]* |
|---|---|---|---|---|---|---|---|
| CuMgAl-LDH | 7.68 | 1.54 | 10.3 | 13.7 | 3.08 | 23.0 | 80 |
| CuMgFe-LDH | 7.62 | 1.56 | 9.8 | 16.1 | 3.12 | 22.9 | 70 |

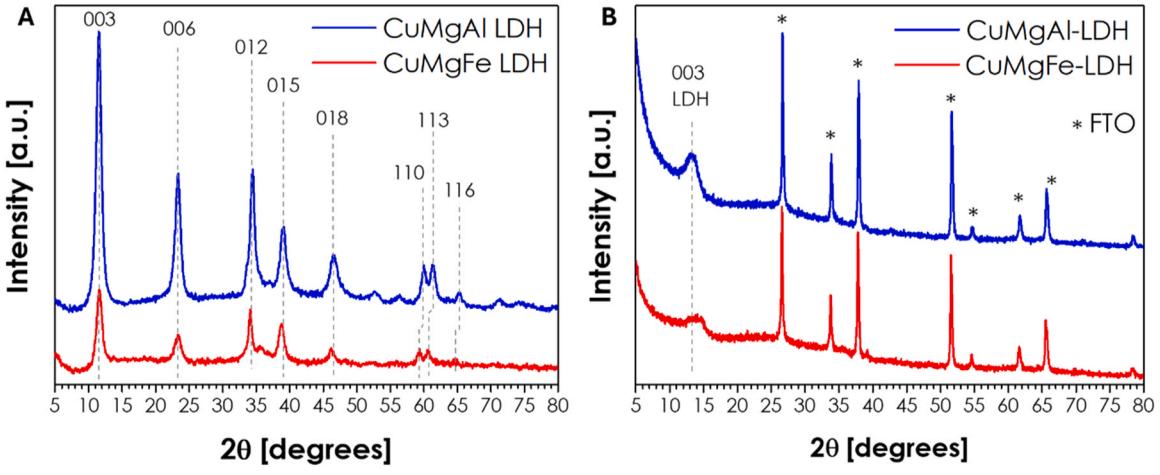


**Fig. 1.** XRD diffraction pattern of powder samples (A) and screen-printed LDH-based films onto FTO (B).

values, 13.3° and 14.0° for CuMgAl-LDH and CuMgFe-LDH respectively, meaning lower d-spacing and thus a contraction of the layered structure. The phenomenon can be assigned to the effect of films' thermal treatment which could affect the crystal order and can cause a partial loss of interlayer crystallization water resulting in diminished interlayer height [94].

Nitrogen physisorption analyses were carried out to determine the specific surface area (SSA) of the synthetized bulk material. The two samples resulted in close value of SSA, as reported in Table 1, in good agreement with the results reported in literature for this kind of materials [63].

Scanning electron microscopy (SEM) was employed to investigate films' morphology and microstructure. The low magnification micrographs, reported in Fig. 2 A, 2D, highlighted an overall homogeneous film deposition even though few micro-cracks are present, especially for CuMgFe-LDH sample. The films microstructures are shown in the higher magnification images (Figs. 2B, 2E). The morphology of the films surface is composed of LDHs' nanoplatelets with a preferential orientation parallel to the substrate, in contrast to the powder particles, which are composed of randomly oriented layered crystallites (Figure S1, Support information). This characteristic could be related to the three-roll mill step during the ink formulation and the deposition method employed, i.e. screen-printing; during milling, the particles can be stretched due to the high shear stress imposed by the zirconia rollers while the screen-printing process forces the particles dispersed in the ink matrix to the most packed orientation, thus resulting in preferred planar orientation of LDH particles, which in turn could benefit the electrical properties of the films [95,96].

Energy dispersive X-ray analyses (EDX) were carried out to confirm the desired atomic ratio between metal elements in the samples. The EDX analyses carried out in different points (Figure S2, Supporting Information) confirmed the ternary nature of the LDH with cations molar ratios reported in Table 2. The experimental results match very well Cu/Mg/M (M=Al, Fe) expected 2:1:1 ratio, while the EDX mapping shown in Fig. 2C-F, showed an optimal dispersion of the elements in the inorganic structure, highlighting an advantage and characteristic of the utilization of LDH, which possess an intrinsic cation interspersion.

To get further insights into the morphology of the samples at the nano dimension the samples powders were analysed by TEM-EDX as reported in Fig. 3. TEM images showed the presence of a lamellar structure in which the layers of the layer double hydroxide emerged. The analysis of the dimension of these layers shows a interlayer distance around 0.6 nm which is compatible with what has been observed by XRD. EDX analysis allowed to identify the distribution of elements in the sample. It confirmed a good interdispersion of Cu, Mg, Al or Cu, Mg, Fe in the samples. In order to further understand the nature of the species present on the surface of the sample, XPS analysis was conducted.

**Table 2 –**
Estimated metals' cations molar ratio determined through punctual EDX analyses.

| *CuMgAl-LDH* | | *CuMgFe-LDH* | |
|---|---|---|---|
| Cu/Mg | 1.94 ± 0.09 | Cu/Mg | 2.1 ± 0.1 |
| Cu/Al | 2.04 ± 0.09 | Cu/Fe | 2.2 ± 0.2 |
| Mg/Al | 1.05 ± 0.05 | Mg/Fe | 1.0 ± 0.1 |
| (Cu+Mg)/Al | 3.1 ± 0.1 | (Cu+Mg)/Fe | 3.2 ± 0.3 |

XPS spectra were acquired for the powders of CuMgAl-LDH and CuMgFe-LDH as well as for the electrodes on FTO. Survey spectra are shown in Figure S3 and all peaks in the range 0–1400 eV were identified and could be assigned to either Cu, Mg, Al, Fe, C, and O, with no signal from the underlying FTO support. Fig. 4 shows the high-resolution spectra acquired for the core levels C *1 s*, O *1 s,* and Cu $2p_{3/2}$ CuMgAl-LDH in the form of powder (bottom) and once deposited on FTO (top). The spectra for the core levels Al *2p* and Al *2 s* were also recorded and are shown in Figure S4, but they suffer from severe overlapping with Cu *3p* and Cu *3 s* peaks, respectively. In the powder, carbon was mainly present as graphitic carbon (BE = 284.8 eV) and bonded with oxygen in carbonate species (BE = 288.9 eV), with a smaller contribution attributable to species containing C-OH or C-OC groups (BE = 286.3 eV).

In the spectra of CuMgAl-LDH/FTO, the intensity peak related to the C-OH and C-O-C bonds containing species (BE = 286.3 eV) increased significantly and a new component attributable to the presence of carbonyl-containing compounds (BE = 287.8 eV) appeared, possibly due residues of the organic components of the ink. The O *1 s* core level spectra were very similar for both the powder and the electrode, being dominated by a peak centred at ~ 531.5 eV attributable to the -OH groups of the layered double hydroxides [97–99]; the binding energies of the O *1 s* core level in metal carbonates also falls in this range [100].

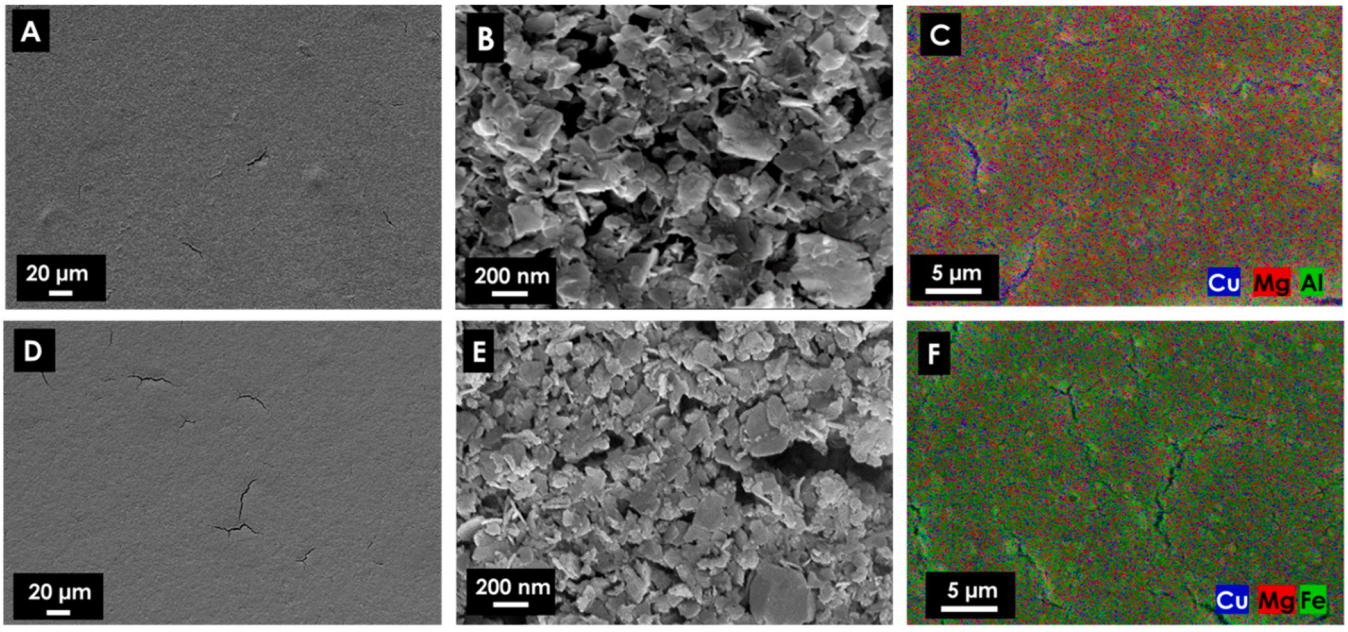


**Fig. 2.** – FE-SEM micrographs at low and high magnification of CuMgAl-LDH (a, b) and CuMgFe-LDH (d,e) electrodes. EDX mapping of CuMgAl-LDH (c) and CuMgFe-LDH (f) samples.

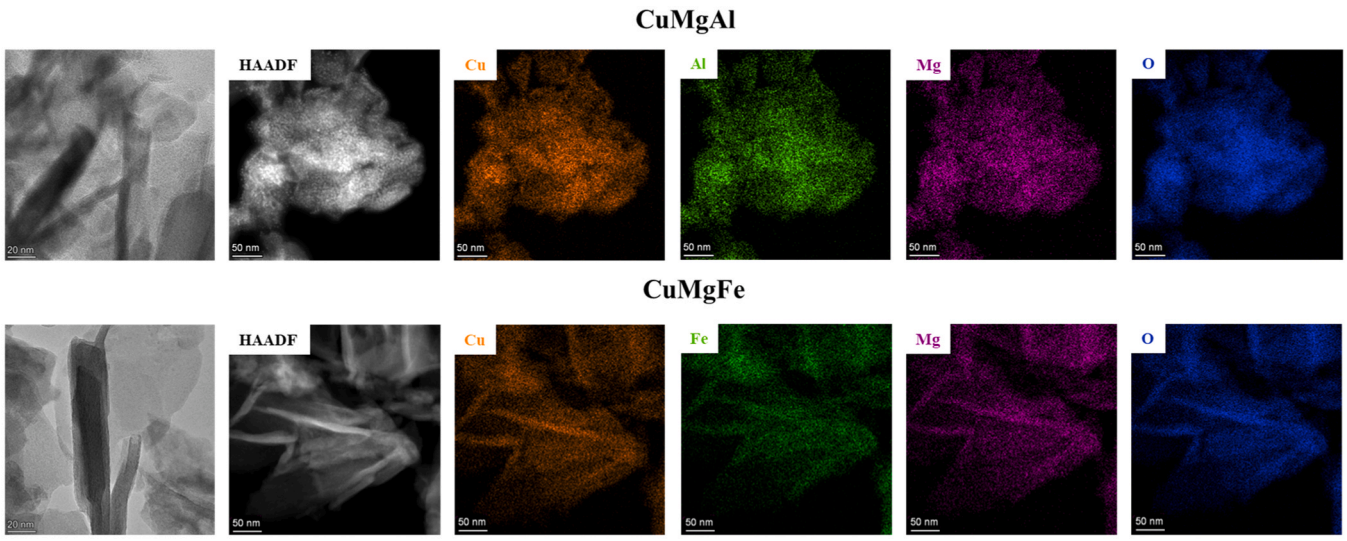


**Fig. 3.** – TEM images and EDS maps obtained on the CuMgAl and CuMgFe samples.

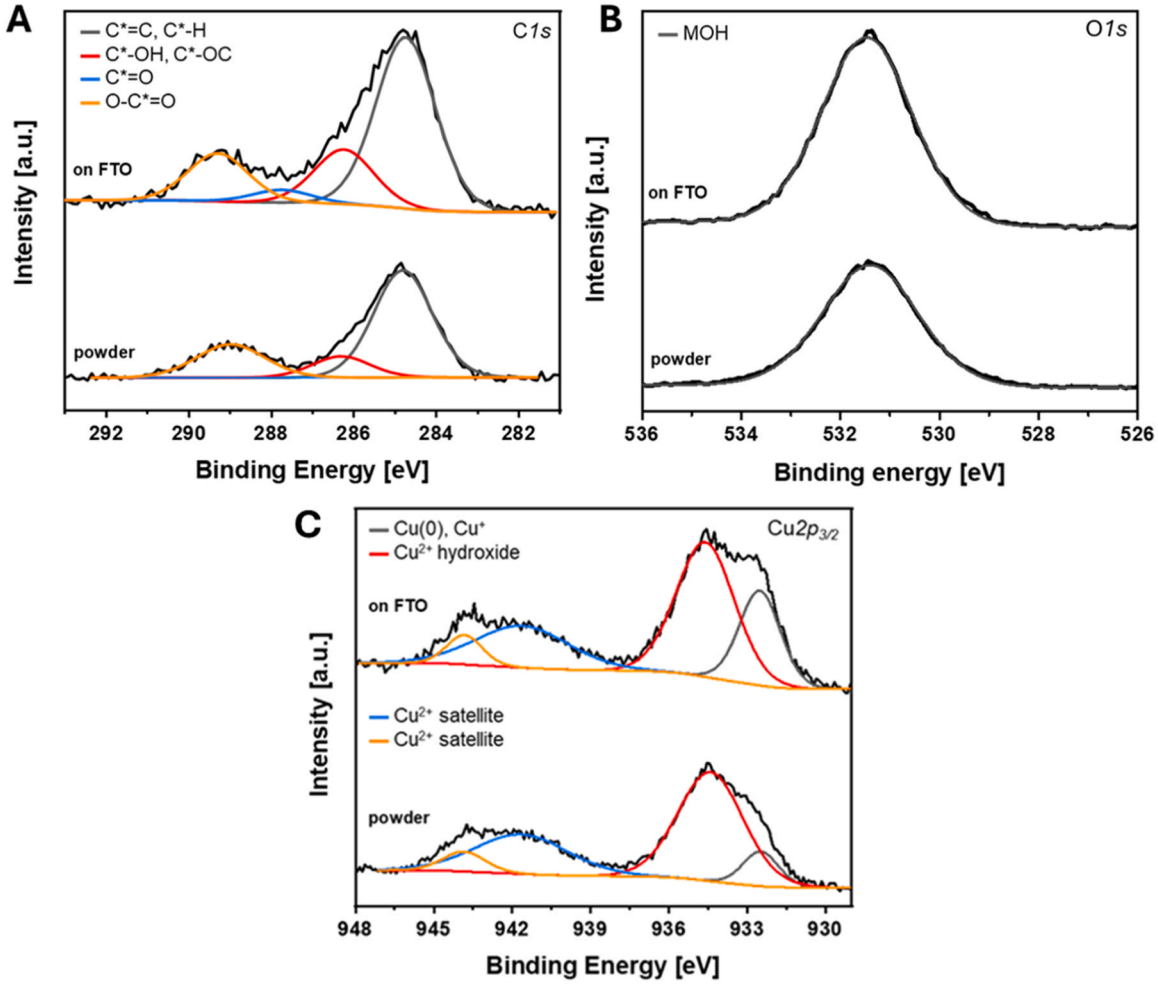


**Fig. 4.** High-resolution XPS spectra of CuMgAl-LDH powder and of CuMgAl-LDH/FTO for the core levels C 1 s (A), O 1 s (B), and Cu $2p_{3/2}$ (C).

Two other small peaks were present at lower binding energy and higher binding energy: the former (529.4–529.7 eV) can be attributed to small amounts of metal oxides, possibly formed due to prolonged exposition to X-ray during XPS; the latter (BE = 533.0 – 533.1 eV) can be attributed to water adsorbed on the surface of the material. The Cu $2p_{3/2}$ core level spectrum of both the LDH powder and electrode showed a major peak (BE = 934.4 eV) attributed to $Cu^{2+}$ hydroxide and a second peak at BE = 932.5 eV corresponding to $Cu^{0}$ and/or $Cu^{+}$ species [101]. The latter signal is known to be generated as a consequence of prolonged X-ray exposure during XPS analysis of $Cu^{2+}$ hydroxides [102]. Satellite peaks

at higher binding energies are shake-up peaks of $Cu^{2+}$. In the attempt to identify the nature of reduced copper spaecies ($Cu^0$ or $Cu^+$), which typically show Cu $2p_{3/2}$ peaks at nearly identical binding energies, we also acquired Cu LMM Auger transition spectra. However, due to the large excess of $Cu^{2+}$, it was not possible to estimate the ratio between Cu (0) and $Cu^+$, as can be seen in Figure S5. Finally, both CuMgAl-LDH and CuMgAl-LDH/FTO displayed one peak (i.e., unresolved Mg $2p_{1/2}$ and Mg $2p_{3/2}$ transitions) centred at BE = 49.8 – 49.9 eV and attributable to magnesium hydroxide (Figure S6a).

Fig. 5 shows the high-resolution spectra acquired for the core levels C *1 s*, O *1 s*, Cu $2p_{3/2}$ and Fe *2p,* for CuMgFe-LDH in the form of powder (bottom) and once deposited on FTO (top). Similarly to CuMgAl-LDH, in the pristine CuMgFe-LDH powder, most of the surface carbon was present as graphitic carbon (BE = 284.8 eV) and bonded with oxygen in carbonate species (BE = 289.3 eV), with smaller contributions attributable to species containing C-OH and C-OC bonds (BE = 286.3 eV) and carbonyl groups (BE = 287.8 eV). Also, in analogy with CuMgAl-LDH/FTO, in CuMgFe-LDH/FTO the intensity of the C *1 s* signals attributable to organic compounds (e.g., 286.3 eV and 287.7 eV) increased possibly due to organic additives remaining from the ink. Also in this case, in the O *1 s* core level spectra, there was a major peak centred at BE = 531.3 eV attributable to the -OH groups and interlayer carbonates of the layered double hydroxides and another component at BE = 529.5–529.6 eV attributable to metal oxides. In analogy with CuMgAl, the spectrum of the Cu $2p_{3/2}$ core level of CuMgFe showed peaks attributable to $Cu^{2+}$ hydroxide (BE = 934.5 eV) and a peak centred at BE = 932.5 eV corresponding to Cu(0) and/or $Cu^+$ species. Remarkably, the analysis showed that the fraction of reduced Cu species in the pristine powder was higher than for CuMgAl-LDH in both powder (e.g., 13.4 mol%) and deposited film (31.3 mol%) forms.

The spectrum of the Fe *2p* core level for the pristine LDH and CuMgFe/FTO was characterized by signals attributable to the presence of $Fe^{3+}$ [103,104] mainly (Fe $2p_{3/2}$ component at BE = 712.2 eV). Again, the Mg *2p* signal of both CuMgFe-LDH powder and electrode (Figure S6b) shows only one peak at 49.8 eV attributable to magnesium hydroxide.

### 3.2. *Physico-chemical and photoelectrochemical characterization of photoelectrodes*

#### 3.2.1. *Optical properties and band characterization*

The optical properties of the prepared photoelectrodes were characterized by UV–vis spectrophotometric analysis for light absorption behaviour and band gap determination. Absorption spectra were collected (Fig. 6A) and the bandgaps were calculated by extrapolating the intercept of the linear section of the Tauc plot (Fig. 6B) obtained by applying Tauc equation (Eq.2, par. 2.4).

The two LDH-based photoelectrodes resulted suitable for UV–vis light absorption as shown by their absorbance spectra in the range 300–800 nm. Fe-containing LDH displayed a wider visible light absorption capacity respect to Al-containing LDH, as confirmed by the calculated band gap energies ($E_g$) which were 2.2 and 2.9 eV for Fe and Al respectively.

Mott-Schottky analysis have been then conducted to determine the

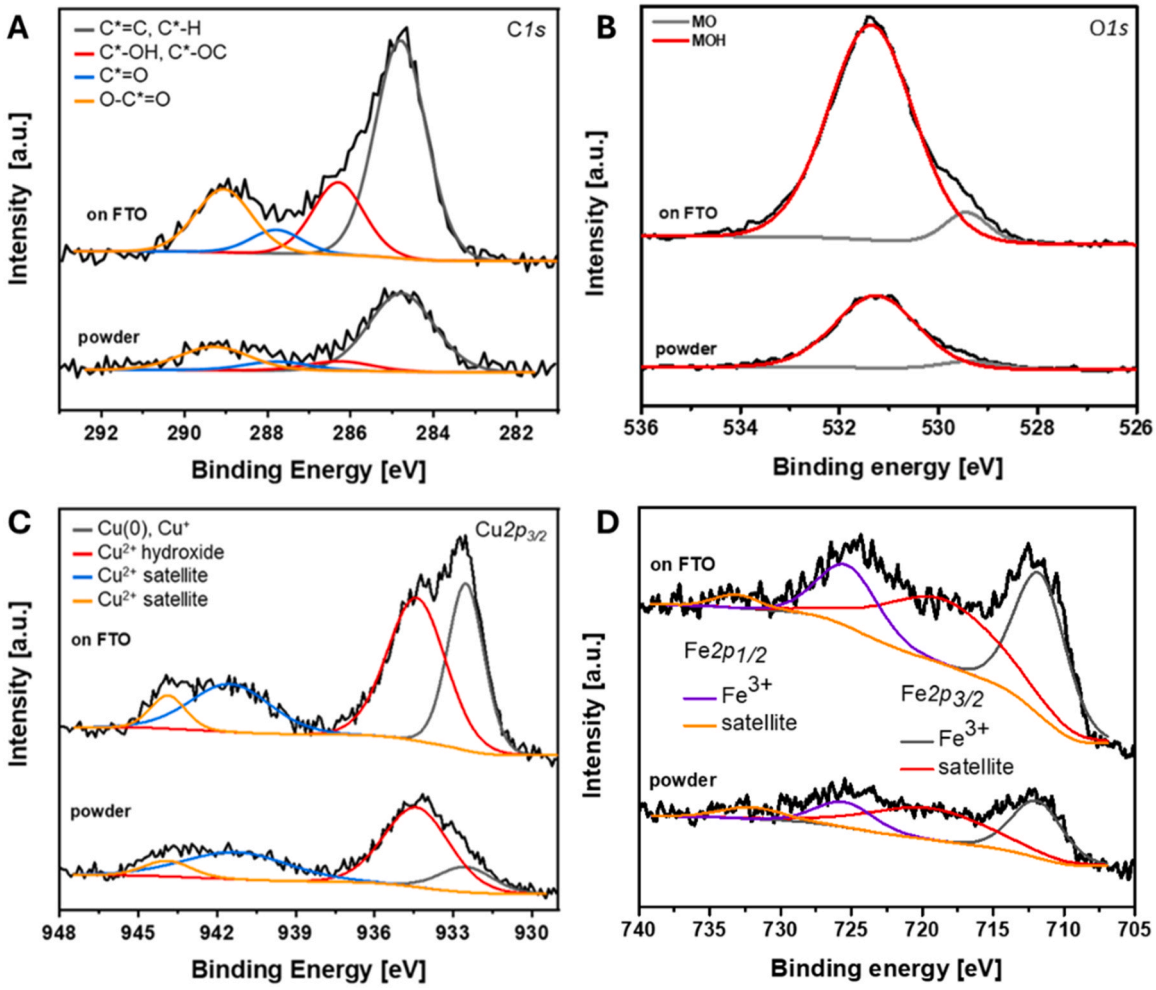


**Fig. 5.** High-resolution XPS spectra of CuMgFe-LDH powder and of CuMgFe-LDH/FTO for the core levels C 1 s (A), O 1 s (B), Cu 2p3/2 (C), and Fe 2p (D).

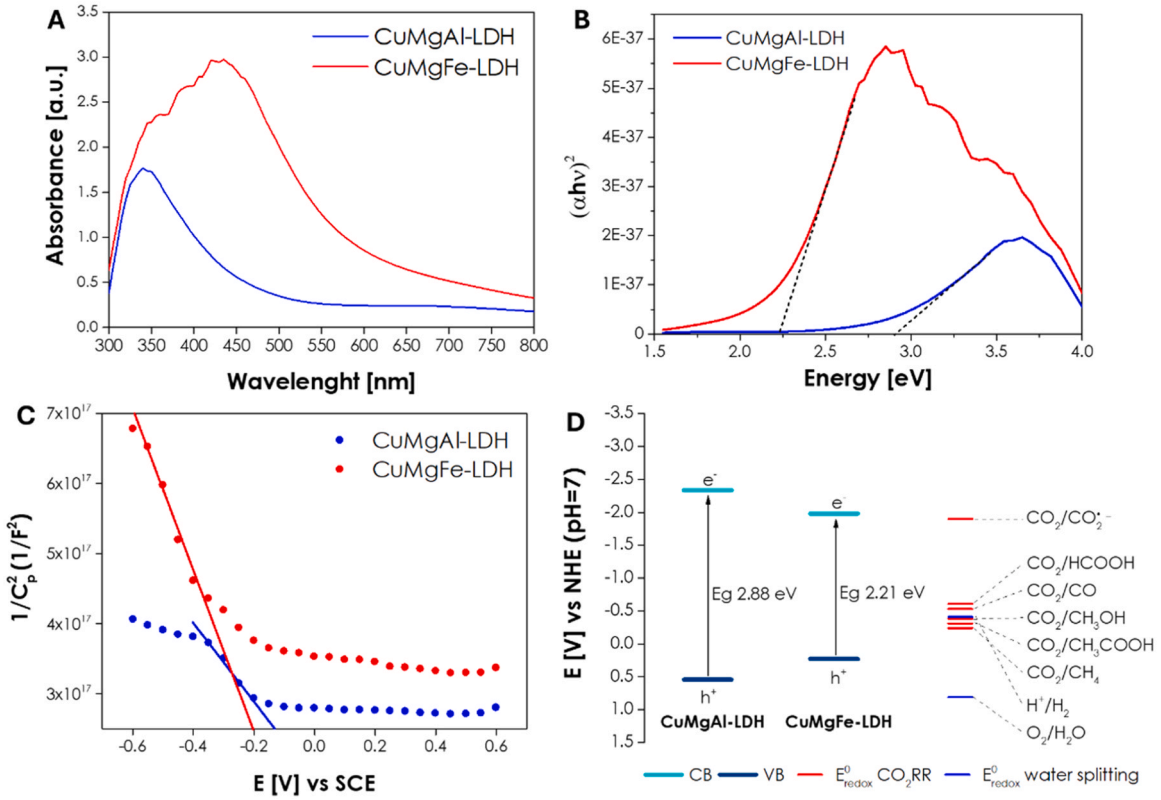


**Fig. 6.** Photo-electrochemical characterization of Cu-based LDH photocathodes: (A) UV−vis-NIR absorption spectrum of Al and Fe-containing CuMgM(III) LDH and (B) corresponding Tauc plots of CuMgAl-LDH and CuMgFe-LDH used for band gaps extrapolation. (C) Mott−Schottky plots collected at frequencies of 47 kHz of the electrodes in 0.1 M $Na_2SO_4$ solution measured in the dark. The x-intercept yields the flat band potential vs SCE. (D) Experimentally determined CuMgAl-LDH and CuMgFe-LDH conduction and valence band edges and thermodynamic redox potentials of $CO_2$ reduction products on a potential diagram, depicting favourable energetics for photo-assisted $CO_2$ reduction.

electronic properties of the materials under examination. In particular this technique allows to determine flat band potential ($V_{fb}$), the number of charge carriers ($N_D$), and the intrinsic doping nature of the semiconductor materials [85,105]. The resulting plots determined by impedance measurements a 47 kHz are reported in Fig. 6 C. It is evident that the slope of the fitting line for the Mott–Schottky plots is negative for both examined samples, indicating that the Cu-based LDHs show p-type semiconductor-like properties. Therefore, the majority of charges present in the electrode are positively charged ($h^+$). In such conditions, when the electrical capacity at the electrolyte/electrode interface (C) is zero, the flat band potential can be considered close to the conduction band of the analysed material. The flat band potential (i.e. energy of the top edge of valence band) of CuMgAl-LDH and CuMgFe-LDH resulted to be 0.54 and 0.23 V vs NHE, respectively. The energy of the bottom of conduction band was calculated thanks to previously determined band gap energy ($E_g$), leading to values of −2.34 V vs NHE for CuMgAl-LDH and −1.98 V vs NHE for CuMgFe-LDH. Thus, the energy level diagram was built up to compare the energy of free charges generated by photoexcitation process with the standard redox potential of many $CO_2$RR, as reported in Fig. 6D. Both the two systems resulted, from a thermodynamic point of view, suitable for $CO_2$ activation and reduction since the energy of electrons in the conduction band is higher than both the initial electron transfer step for $CO_2^{\bullet -}$ formation (rate determining step) [106,107] and $E^0_{redox}$ of $CO_2$RR products formation.

LSV measurements were carried out to evaluate the current density produced by the samples in dark conditions, as well as the photocurrents in case of illumination with a solar simulator (1 sun, AM 1.5, 1000 W $m^{-2}$). As shown in Fig. 7 A, both CuMgAl-LDH and CuMgFe-LDH based photoelectrodes achieved higher cathodic current densities when illuminated, with respect to dark measurements, proving their photo-electrode character. The Faradaic peaks observed at 0.18 V in dark curve and 0.35 V in light curve for CuMgAl-LDH can be ascribed to the reduction of surface Cu oxides locally formed during LSV measurements, with the first related to Cu(I)/Cu(0) reduction process and the second to the reduction of Cu(II) to Cu(I) [108,109]. On the other hand, the cathodic peaks appearing in the light LSV of CuMgFe-LDH at 0.07 V and −0.15 V vs RHE can be attributed to reduction process of Fe(III) oxides and oxyhydroxides (formed during the LSV measurements and already present in LDH phase) to $Fe(OH)_2$ and of $Fe(OH)_2$ to metallic iron, respectively [110,111]. Interestingly, the Fe-containing LDH showed a higher current density developed during the scanning of cathodic potential, both in dark and under illumination conditions, suggesting a better conductivity respect to the Al-containing one. The transient photocurrent densities were shown in Fig. 7B. CuMgFe-LDH showed a transient photocurrent density 4 times higher than that generated by CuMgAl-LDH, in agreement LSV profiles. The beneficial effect of Fe presence in the structure was further confirmed by Electrochemical Impedance Spectroscopy (EIS) analysis. The measurements were conducted at two distinct potentials of interest. In order to evaluate the true behaviour of electrodes in terms of corresponding electrode-electrolyte charge transfer resistance ($R_{ct}$), while reducing possible complexities related to applied bias and current flow, the measurement was firstly conducted in equilibrium condition, i.e. at the open circuit potential (OCP) determined for each electrode [112,113]. Secondly, for a more realistic comparison in terms of $R_{ct}$ values, EIS analyses were made at constant potentials in the catalytic turnover conditions where the whole interface performs the desired electrocatalytic reaction, i.e. −0.4 V vs RHE [114]. The experimental curves could be fitted with the equivalent circuits indicated in the inset of Fig. 7C-D.

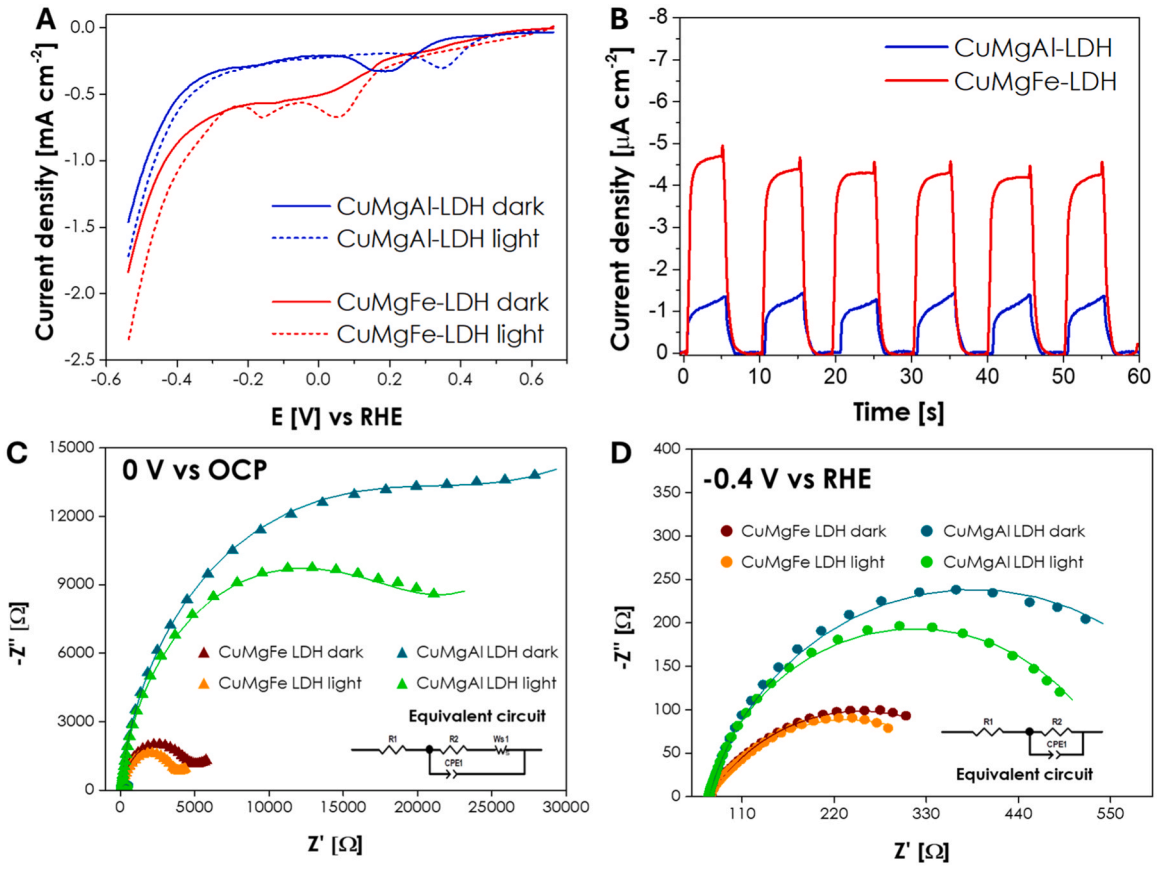


**Fig. 7.** – Charge-transfer properties of Cu-based LDH photocathodes: (A) LSV curves in dark (solid line) and under illumination (dashed line) of CuMgAl-LDH and CuMgFe-LDH in 0.1 M KOH electrolyte purged with Ar (scan rate: 10 mV $s^{-1}$). (B)Transient photocurrent response. (C) Nyquist's plots of CuMgAl-LDH and CuMgFe-LDH electrodes at OCP and (D) at −0.4 V (vs. RHE) in the dark and under illumination conditions in $CO_2$-saturated 0.3 M $KHCO_3$ aqueous solution.

In such circuits $R_s$ encompasses all resistances linked to the electrochemical system (electrolytic solution, wires, electrical contacts) while $R_{ct}$ accounts for charge-transfer resistance at the interface between electrode and electrolyte and CPE1 (constant phase element), represents the capacitance for charge accumulation at the double-layer region. Finally, Ws1 (Warburg short diffusion element) represents the diffusion of mobile charges within electrodes and in solution [115]. As evidenced by Nyquist's plot reported in Fig. 7 C, the charge-transfer resistance of CuMgFe-LDH has been found to be significantly lower than that of CuMgAl-LDH, i.e. 4.40 ± 0.06 vs 21.4 ± 0.9 kΩ in dark and 3.67 ± 0.04 vs 18.5 ± 0.6 kΩ under illumination at equilibrium condition (OCP). Moreover, the impedance spectra recorded under light exhibit smaller arches compared to the corresponding dark curves. This indicated that the sample's charge transfer capability is heightened due the increased number of charges generated from the photoexcitation process. Although the same considerations remain valid the results of impedance measurements at −0.4 V vs RHE it is interesting to note that the relative difference in $R_{ct}$ between the two samples diminished remarkably upon application of cathodic bias as reported in Table 3. Electrochemical surface area (ECSA) of the prepared photocathodes was estimated by CV measurements conducted at various scan rates, as depicted in Figure S7. As expected, CuMgFe-LDH photocathodes resulted in a 2 time higher ECSA respect to CuMgAl-LDH, respectively 100.6 ± 0.2 and 48.9 ± 0.2 $cm^2$.

From Fig. 8, the CuMgFe-LDH photoelectrode showed a higher IPCE value than CuMgAl-LDH one due to its better charge collection and reduced recombination phenomena that finally enhanced the amount of photocurrent produced confirming the results obtained from LSV analyses.

At high potential applied (-0.8 V vs RHE), higher charge lifetime was observed for CuMgFe-LDH photoelectrode than the one obtained for CuMgAl-LDH, and lifetime was found to be about 0.24 e 0.10 s for the iron and magnesium-based systems respectively. However, at lower potential applied the trend was inverted, probably due to the different energy levels (conduction and valence band position) of LDH based photoelectrodes. Considering the chemical capacitance, CuMgFe-LDH showed highest values in all potential range investigated, due to its different spatial distribution of electrons traps linked to its microstructure and surface area. The, for CuMgFe-LDH a reduced recombination rate and the improved charge transport properties were observed confirming the results previously obtained from the other characterizations.

**Table 3**
Charge-transfer resistances of CuMgAl-LDH and CuMgFe-LDH photoelectrodes under dark and illumination conditions at two different applied bias (OCP and −0.4 V vs RHE).

| *Sample* | *Rct (kΩ) at OCP (0.6 V vs RHE)* | | *Rct (kΩ) at – 0.4 V vs RHE* | |
|---|---|---|---|---|
| | dark | Light | dark | Light |
| CuMgAl-LDH | 21.4 ± 0.9 | 18.5 ± 0.6 | 0.631 ± 0.007 | 0.494 ± 0.003 |
| CuMgFe-LDH | 4.40 ± 0.06 | 3.67 ± 0.04 | 0.361 ± 0.005 | 0.330 ± 0.005 |

### 3.3. *Photoelectrocatalytic CO2 reduction*

PEC $CO_2$ reduction performance evaluation of the prepared photocathodes was evaluated by a potential screening approach to identify and quantify the reduction products generated from $CO_2$ by using progressively higher cathodic potentials. For this purpose, potentials of 0, −0.4 and −0.9 V vs RHE were chosen for the screening.

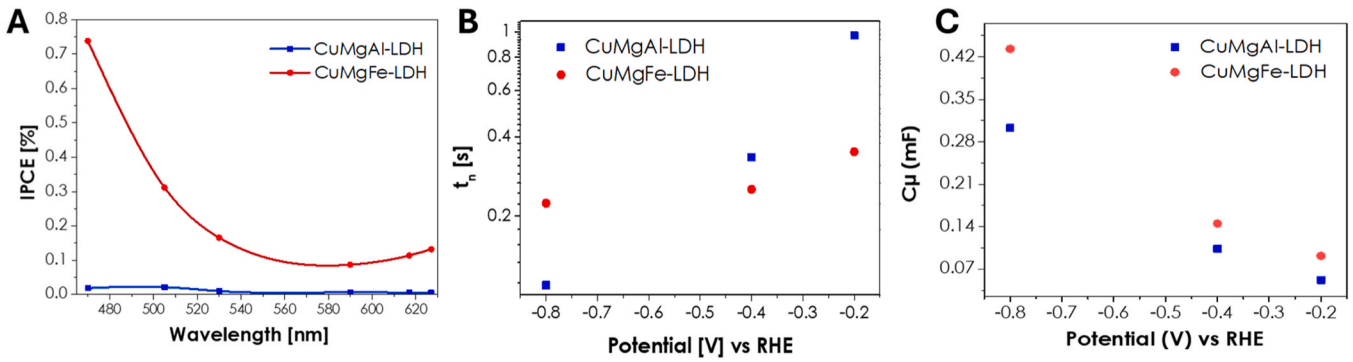


**Fig. 8.** (A) Incident photon-to-current conversion efficiency (IPCE) for CuMgAl-LDH and CuMgFe-LDH photoelectrodes. (B) Charge-carrier lifetime ($\tau_n$) and (C) chemical capacitance ($C_\mu$) determined by EIS analyses in dark in function of different potentials applied.

### 3.3.1. *CuMgAl-LDH*

The distribution of $CO_2$RR products obtained with CuMgAl-LDH is illustrated in Fig. 9 A.

A similar screening has been previously performed by our research group with electrosynthesized CuMgAl LDH for $CO_2$ electrochemical reduction ($CO_2$ER) [62]. There, −0.4 V vs RHE was recognized as the most suitable potential to maximize acetic acid selectivity and productivity while keeping low hydrogen production which was conversely favoured at a higher applied potential, i.e. −0.8 V vs RHE. Moreover, no $CO_2$RR products were detected under the application of a less cathodic potential such as −0.2 V vs RHE. In this work, the chemically synthetized CuMgAl-LDH catalyst has displayed further interesting results, firstly confirming the profitable activity toward $CO_2$ conversion into acetic and formic acid, but also into ethanol. Photocurrent density achieved and products' formation rate are reported in Table 4. Surprisingly, respect to the previously reported results, electrode illumination coupled with the application of an external bias of 0 V vs RHE, was sufficient to yield (i) current density close to that reported for $CO_2$ER with electrodeposited CuMgAl-LDH at −0.4 V vs RHE; (ii) a relevant amount of acetic acid, i.e. 0.44 μmol $h^{-1}$ $cm^{-2}$, only slightly lower than that obtained with electrodeposited CuMgAl-LDH (0.53 μmol $h^{-1}$ $cm^{-2}$) in dark $CO_2$ER; (iii) a doubled acetic acid productivity than that obtained in our PEC system with a bias of −0.4 V vs RHE, i.e. 0.21 μmol $h^{-1}$ $cm^{-2}$. Therefore, this operational condition resulted as the most selective for acetic acid production as testified by faradaic

**Table 4**
PEC $CO_2$RR products' formation rate and photocurrent density under screened applied potentials for CuMgAl-LDH.

| *E [V] vs RHE* | *J [mA $cm^{-2}$]* | *$H_2$ [μmol $h^{-1}$ $cm^{-2}$]* | *$CH_3COOH$ [μmol $h^{-1}$ $cm^{-2}$]* | *HCOOH [μmol $h^{-1}$ $cm^{-2}$]* | *$CH_3CH_2OH$ [μmol $h^{-1}$ $cm^{-2}$]* |
|---|---|---|---|---|---|
| 0 | -0.34 | n.d. | 0.44 | 0.59 | 0.10 |
| - 0.4 | -0.60 | 6.8 | 0.21 | 0.58 | 0.10 |
| - 0.9 | -5.4 | 98 | 0.22 | 6.50 | 0.10 |

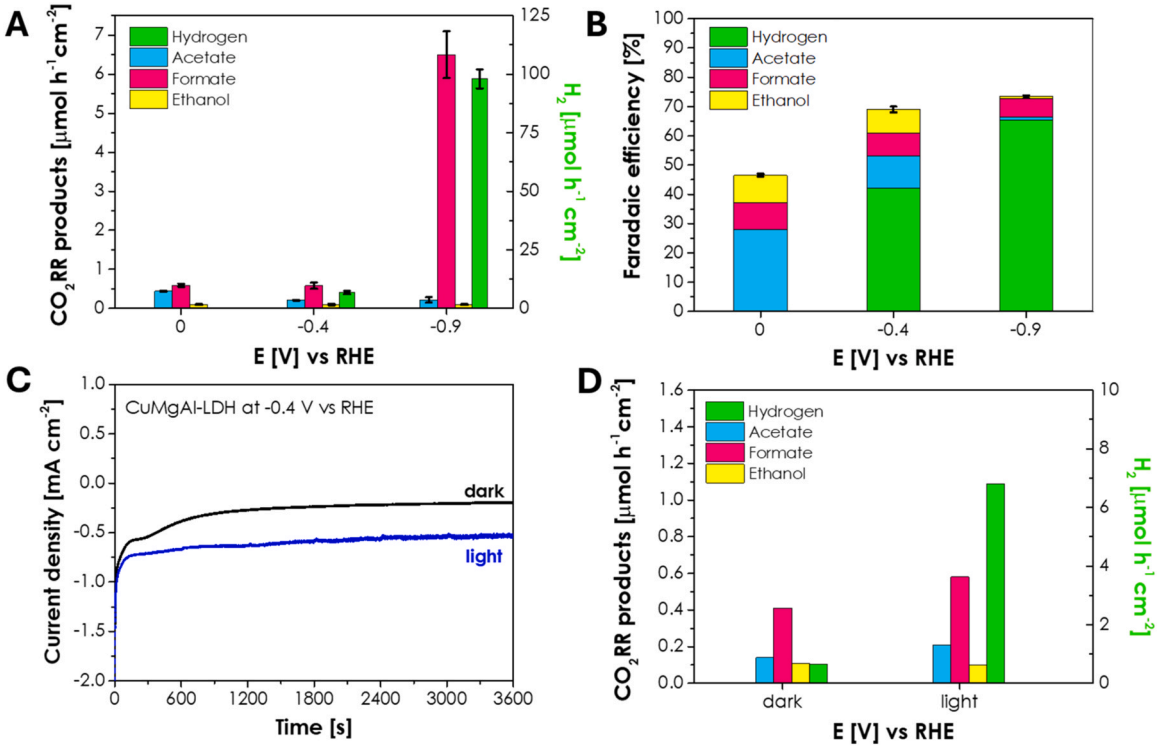


**Fig. 9.** PEC $CO_2$RR products distribution for a 1 h reaction at different applied potentials using the CuMgAl-LDH catalyst: productivity (A) and faradaic efficiency (B). Current density profiles of PEC test in dark and under light condition for 1 h at −0.4 V vs RHE (C) and relative products formation rate (D).

efficiency increase from 11 % at −0.4 V vs RHE to 28 % at 0 V vs RHE. These results may be attributed to the photovoltage generated through LDH illumination which in turn is traduced in lower external energy (applied bias) requirement [116]. Besides acetic acid, also a relevant amount of formic acid and trace of ethanol were detected at 0 and −0.4 V vs RHE with a quite constant productivity among the two conditions.

Lastly, it was observed that at the most cathodic potential (-0.9 V), the only $CO_2$RR products that benefit for higher reductive condition was formic acid which reached a yield of 6.5 μmol $h^{-1}$ $cm^{-2}$, and again a quite similar yield of acetic acid and ethanol was recorded with respect to −0.4 V vs RHE tests. In terms of selectivity the favoured product under the most cathodic potential was formic acid paired with a prominent hydrogen evolution.

In these tests, at low voltage mainly acids are obtained, with a high faradaic efficiency in $C_2$ products and particularly to acetic acid. At intermediate voltage the acetic acid fraction lowers and hydrogen becomes the predominant product. At further higher potentials a high faradaic efficiency in hydrogen is observed together with still a relevant production of formic acid. Therefore, at low applied potentials and relatively low current density the system is relatively selective for $CO_2$ reduction over HER since the limited electrons are distributed among various $CO_2$ reduction pathways, producing a mixture of formate, acetate, and ethanol. On the other hand, at high current density produced by the application of more cathodic bias, the kinetics of the HER and the 2-electron formate pathway are much faster and scale efficiently with the higher electron supply. In contrast, the C-C coupling pathways to form acetate and ethanol are complex, multi-step processes that are kinetically limited.

Dark $CO_2$ electrolysis test was performed to proof the advantage of activating CuMgAl-LDH catalyst with light. The current density evolved at −0.4 V vs RHE in dark conditions (-0.3 mA $cm^{-2}$) was found to be half than the corresponding measurement under light irradiation as depicted in Fig. 9 C. This enhancement was reflected by reaction products amount increase as reported in Fig. 9D, confirming PEC strategy as a valid approach to lower the external energy input for the electrocatalytic transformation.

### 3.3.2. CuMgFe-LDH

Fig. 10A shows product distribution obtained using CuMgFe-LDH as photocathode for $CO_2$RR and yields are reported in Table 5. At lower cathodic applied potential, i.e. 0 V vs RHE, CuMgFe-LDH shown a photoelectrocatalytic activity very similar to CuMgAl-LDH photocathode, both in terms of productivity and selectivity, with formic and acetic acid as major products, 0.66 and 0.44 μmol $h^{-1}$ $cm^{-2}$ respectively, and minor amount of ethanol (0.10 μmol $h^{-1}$ $cm^{-2}$). Under this condition, no hydrogen was detected with Fe-containing sample, as already noticed for Al-containing one.

Surprisingly, a greater difference in reaction outcome was observed under the application of −0.4 V vs RHE. In this case, CuMgFe-LDH was found not only to perform slightly better than CuMgAl-LDH in terms of formic acid, acetic acid and ethanol yields, but produced also a $C_3$-compound, i.e. 1-propanol in comparable amount with ethanol, 0.12 and 0.14 μmol $h^{-1}$ $cm^{-2}$, respectively. Moreover, according to photoelectrochemical characterization results, at −0.4 V vs RHE, Fe-containing sample developed a larger current density of −1.0 mA $cm^{-2}$, respect to Al-containing sample (-0.60 mA $cm^{-2}$).

Finally, under the most cathodic applied potential, formic acid was identified as the main $CO_2$RR product with a yield of 0.37 μmol $h^{-1}$ $cm^{-2}$, which was greatly lower than that obtained for CuMgAl-LDH. The reason behind this difference could be found in the higher hydrogen evolution, 138.0 μmol $h^{-1}$ $cm^{-2}$ for CuMgFe-LDH vs 98 μmol $h^{-1}$ $cm^{-2}$ for CuMgAl-LDH, which is attributed to improved kinetics derived by

**Table 5**
$CO_2$RR products' formation rate and photocurrent density under screened applied potentials for CuMgFe-LDH.

| *E [V] vs RHE* | *J [mA $cm^{-2}$]* | *$H_2$ [μmol $h^{-1}$ $cm^{-2}$]* | *$CH_3COOH$ [μmol $h^{-1}$ $cm^{-2}$]* | *HCOOH [μmol $h^{-1}$ $cm^{-2}$]* | *$CH_3CH_2OH$ [μmol $h^{-1}$ $cm^{-2}$]* | $CH_3(CH_2)_2OH$ [μmol $h^{-1}$ $cm^{-2}$] |
|---|---|---|---|---|---|---|
| 0 | -0.44 | n.d. | 0.44 | 0.66 | 0.10 | n.d. |
| - 0.4 | -1.0 | 6.5 | 0.30 | 0.69 | 0.14 | 0.12 |
| - 0.9 | -12 | 138 | 0.02 | 0.37 | 0.10 | n.d. |

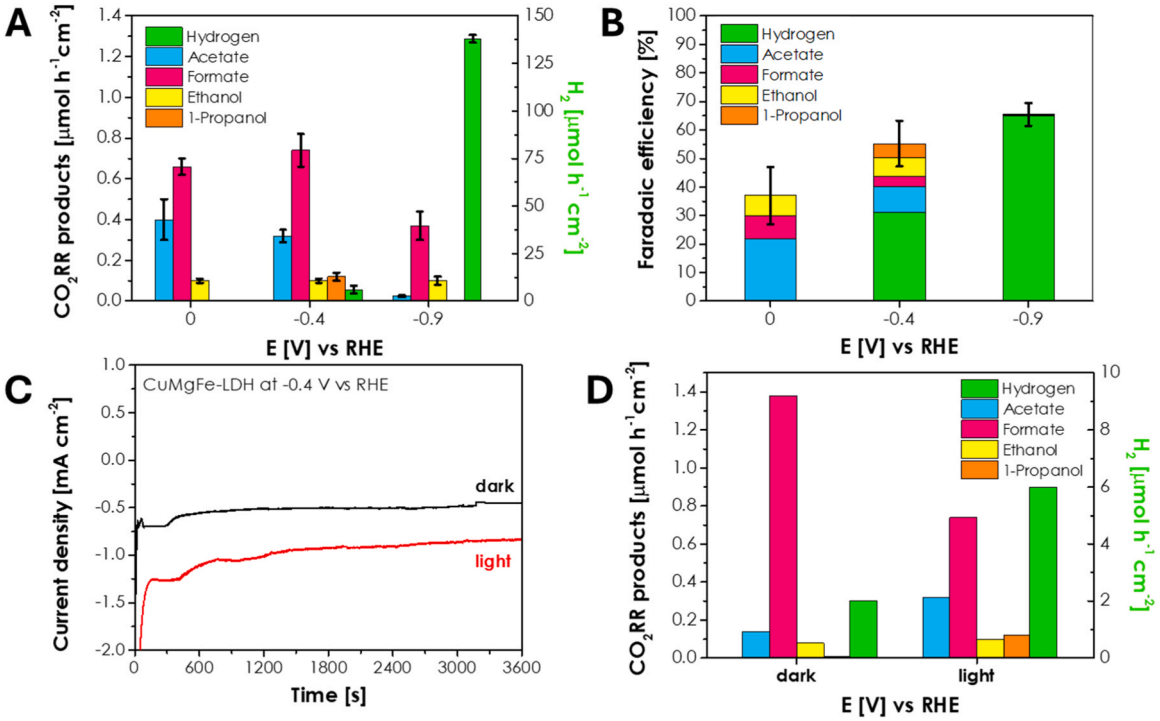


**Fig. 10.** PEC CO2RR products distribution for a 1 h reaction at different applied potentials using the CuMgFe-LDH catalyst.

higher electrons supply at the interface of the photoelectrode and to the iron presence which is widely recognized as a good catalyst for HER promotion [117,118].

Even under this more negative applied bias, the recorder current density for Fe-containing photocathode resulted doubled respect to its Al-containing counterpart, −12 mA $cm^{-2}$ and −5.4 mA $cm^{-2}$, respectively.

At low voltages less reduced liquid products such acids are prevalently produced with higher faradaic efficiency for acetic acid and with a small presence of ethanol. At intermediate voltage the production of acetic acid diminishes and that of formic acid increases, with an increase of more reduced compound such $C_{2+}$ alcohols, together with the beginning of hydrogen evolution. At high voltage still some $CO_2$ derived products are observed but hydrogen is the predominant product. So, we can identify two interesting conditions, the first at low potential with high faradaic efficiency in acetic acid and at intermediate voltage where the faradic efficiency toward $C_{2+}$ products is predominant among liquid products, with alcohols accounting for almost half of the faradaic efficiency for $C_{2+}$ products.

As for CuMgAl-LDH photoelectrodes, dark $CO_2$ electrolysis test was performed. Even for CuMgFe-LDH the current density produced at −0.4 V vs RHE under light conditions was doubled respect to dark electrolysis test which provided a current density of −0.5 mA $cm^{-2}$ as depicted in Fig. 10C. In this case $C_{2+}$ formation mostly benefits for light activated electrode with acetic acid, ethanol and 1-propanol productivity increase in PEC $CO_2$ electrolysis (Fig. 10D). As already discussed, formic acid and hydrogen are the kinetically favoured products of the process due to 2 $H^+/e^-$ transfer requirement. We can notice that formic acid production was higher in dark condition while the evolution of hydrogen increased by a smaller factor respect to what observed for CuMgAl-LDH photoelectrode ($H_{2,\ light}/H_{2,\ dark}$ equal to 1.3 and 3.5, respectively). Therefore, the higher current density developed by light activation did not yield a simply boost in easy to form compounds while provided much electrons for multistep reduction reactions to form $C_{2+}$ acid and alcohols. These results strengthen our idea that Fe-containing LDH provide more suitable active sites for complex reactions to form $C_{2+}$ products at relatively low current density.

### 3.4. Study of the effect of M(III) in LDH-based photocathode

The different products yield and distribution obtained at −0.4 V vs RHE, further prompts to investigate the effect of M(III) on the physicochemical properties of the prepared photocathodes, which in turn could had affected the catalytic activity. Indeed, variations in catalytic activity of the materials are expected to be correlated with the photocurrent generated and with the truly catalytic active sites involved in the reaction. The products yield of PEC $CO_2$ reduction at −0.4 V vs RHE under simulated solar light catalysed by CuMgAl-LDH and CuMgFe-LDH are compared in Fig. 11.

In these conditions the two examined photocathodes were active in $CO_2$ conversion toward organic acids (formic and acetic acids) and alcohols (ethanol); in the case of CuMgFe-LDH, also propanol was formed. As expected from the photoelectrochemical characterization, higher light absorption and conductivity, and lower charge-transfer resistances resulted in a higher current density evolved by CuMgFe-LDH (-1.0 mA $cm^{-2}$) with respect to CuMgAl-LDH, (-0.6 mA $cm^{-2}$) during the reaction. Formic acid and ethanol yields were slightly higher for the CuMgFe-LDH catalysts. However, the most interesting difference was the enhanced productivity of acetic acid and propanol promoted by Fe-containing sample respect to Al-containing one.

To deeply understand the reason of superior activity of CuMgFe-LDH, some morphological and structural characterization have been performed over the spent electrodes. Firstly, XRD analysis revealed that after 1 h reaction under a cathodic potential of −0.4 V vs RHE the materials faced some changes in phases. The diffractograms reported in Fig. 12 present diffraction peaks characteristic of $Cu_2O$ phase (ICSD

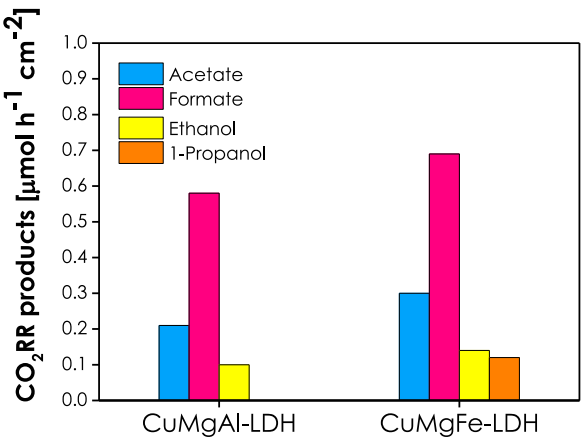


**Fig. 11.** photoelectrochemical $CO_2$RR liquid products obtained after 1 h at −0.4 V vs RHE in 0.3 M $KHCO_3$ electrolyte solution.

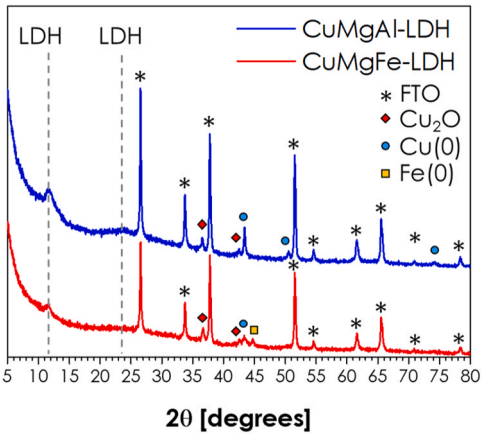


**Fig. 12.** XRD patterns of catalytic films after 1 h of reaction under −0.4 V vs RHE in $KHCO_3$ 0.3 M.

63281) as well as metallic Cu (ICSD 43493) and Fe (ICSD 185753), aside to LDH phase's 003 reflex. The 36.6 ° and 42.5 ° diffraction peaks correspond to the (111) and (002) lattice planes of the $Cu_2O$ phase, and the 43.3° diffraction peak corresponds to the (111) lattice planes of the metallic Cu phase, respectively [108,119,120]. In the CuMgFe-LDH sample, a reflection at 44.7° also appears, which is related to (011) lattice planes of metal iron. The reflections located at 36.6° and 42.5° could also be attributed to FeO phase [121]; nonetheless, complementary characterizations have been employed to confirm this hypothesis. Noteworthy, the intensity of $Cu^0$ related reflection for CuMgAl-LDH is higher than for CuMgFe-LDH while also 50.5° (200) and 74.1° (220) diffraction peaks can be appreciated. To confirm the presence of copper oxide species, Raman spectrum (Figure S8c) of CuMgAl-LDH spent revealed 145, 211, 607 $cm^{-1}$ peaks which can be associated to $Cu_2O$ while those at 279 and 334 $cm^{-1}$ are attributed to CuO [62,108]. Spent CuMgFe-LDH (Figure S8d) displays two bands at 151 and 620 $cm^{-1}$ consistent with those of the $Cu_2O$ phase, while the bands centred at 288 and 338 $cm^{-1}$ indicate the presence of CuO.

FE-SEM and EDX were employed to highlight the different transformation undergone by the two materials during reaction. The first difference between the two samples was the lower extent of structural change occurred for CuMgAl-LDH photoelectrode. However, for CuMgAl-LDH the ubiquitous presence of lamellar particles, shown in Fig. 13 C, suggests only a partial modification of the material structure. On the other hand, the high magnification FE-SEM images of spent CuMgFe-LDH photocathode in Fig. 13 F and 13 G revealed a quite

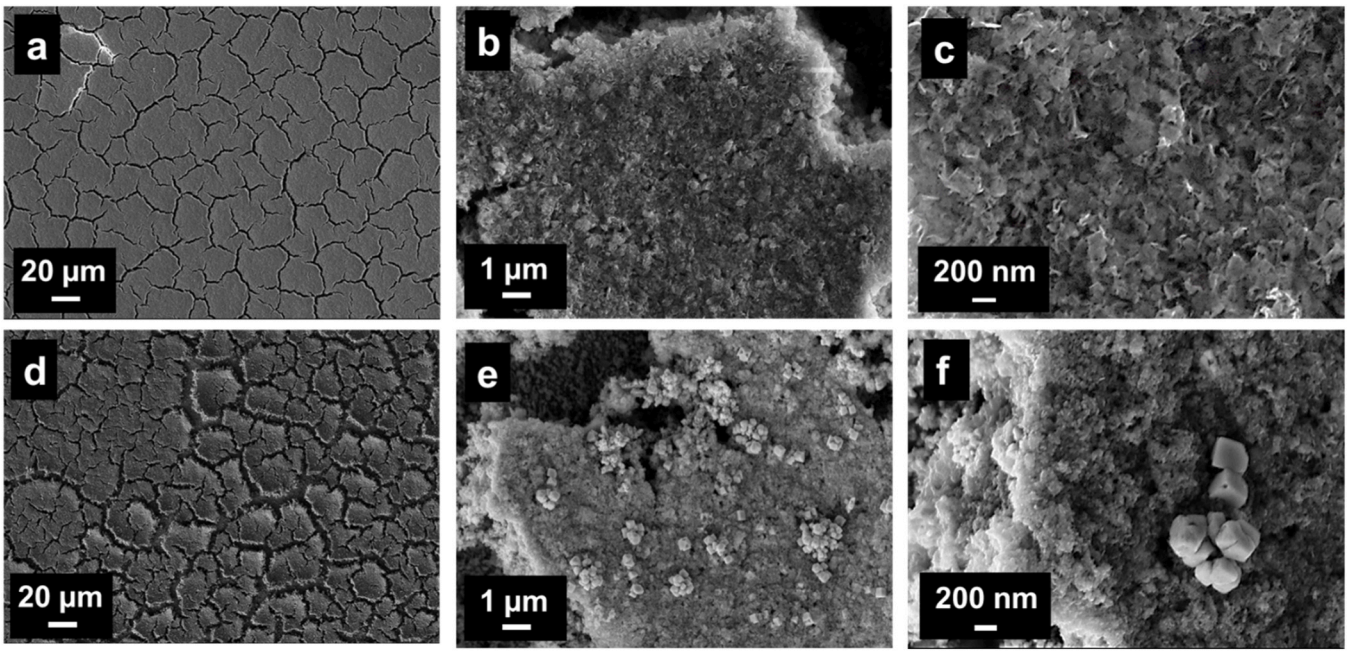


**Fig. 13.** FE-SEM images of spent photocathodes: microscopic view of CuMgAl LDH (a) and CuMgFe LDH (d) films; medium (b) and high magnitude (c) image of CuMgAl-LDH film still presenting lamellar morphology; evidence of morphology changes and segregation resulting from medium (e) and high magnification (f) image of nanostructures formed on CuMgFe-LDH film.

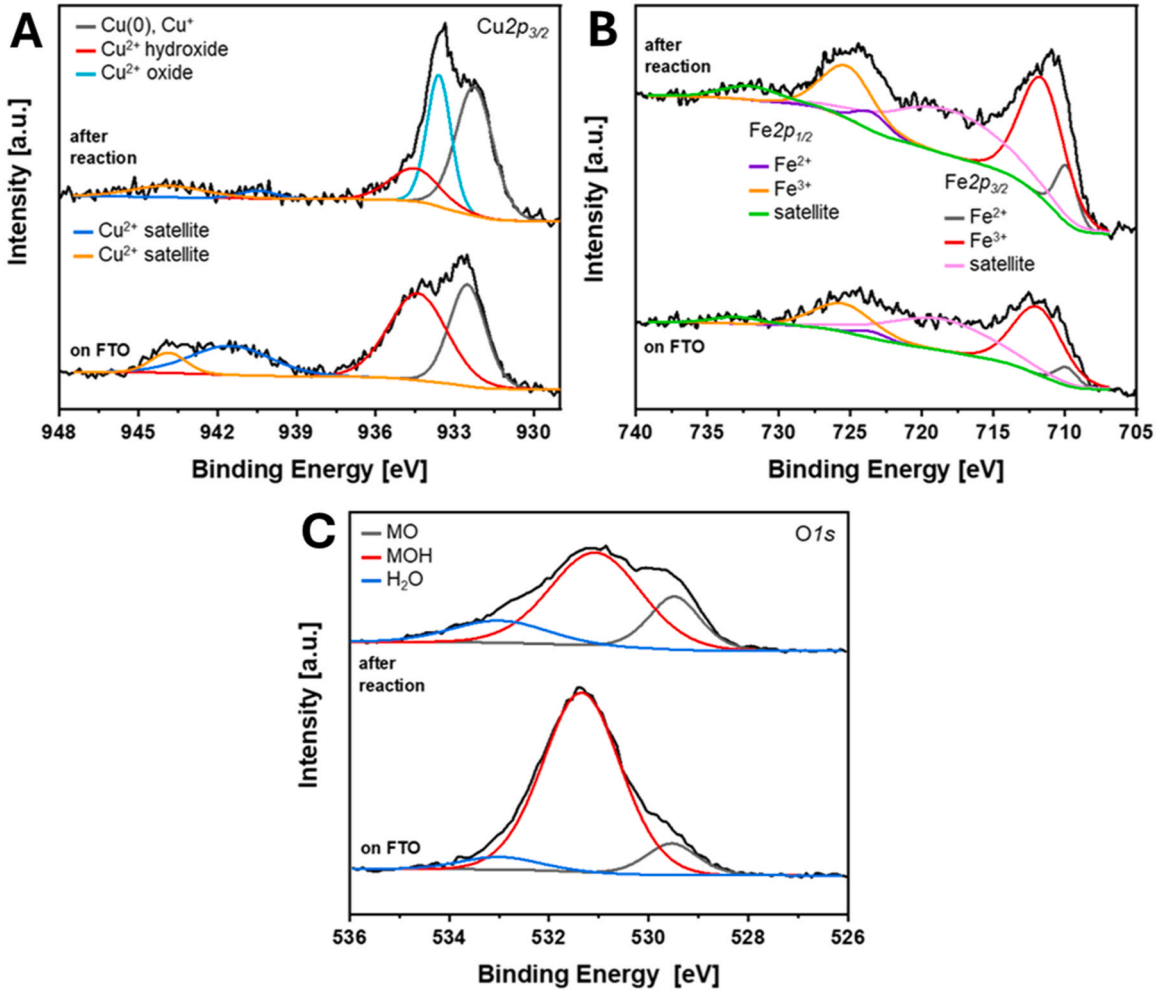


**Fig. 14.** High-resolution XPS spectra of CuMgFe-LDH/FTO fresh and after reaction for the core levels Cu $2p_{3/2}$ (top left), Fe 2p (top right) and O1s (bottom).

different behaviour for Fe-containing LDH. A larger phase transformation occurred, as evidenced by the formation of nanostructures on the surface of the photocathode. Cubic nanoparticles aggregates have been observed and a rich Cu content was determined by EDX punctual analysis (Figure S9). This information, coupled with XRD and Raman analysis allows ascribing such morphologies to $Cu_xO$ species.

XPS characterization after photoelectrochemical tests, which focused on reducible phases elements (Cu, Fe and relative (hydro)oxides), substantially confirmed the results obtained by previous characterizations. The results in figure S10 showing the high-resolution spectra acquired for the core levels O *1 s* and Cu*2p*$_{3/2}$ of CuMgAl-LDH/FTO fresh and after photoelectrochemical testing strongly suggest that the nature of copper redox active centres did not undergo substantial modifications.

On the other hand, Fig. 14 showing the high-resolution spectra acquired for the core levels O *1 s*, Cu *2p*$_{3/2}$, and Fe *2p* for CuMgFe-LDH/FTO fresh and after photoelectrochemical testing indicates that major modifications occurred on the surface of the Fe-containing catalyst.

The O *1 s* core level spectrum after reaction displayed a stronger contribution of the component centered at BE = 529.5 eV (O bonded to metal in oxides) as well as the presence of adsorbed water (BE = 533 eV). In particular, quantitative analysis showed that the surface oxygen in M-O-H groups (BE = 531.3 eV) decreased from 92.9 % to 63.5 %, while those of oxygen bonded to metals in oxides increased from 10.0 % to 20.9 % and from 7.1 % to 20.9 %. This finding points toward a (partial) modification of the LDH structure due to the electrochemical test. These results correlate with the outcome of XRD and Raman spectroscopy (e.g., the partial segregation of Cu and Fe into CuO, $Cu_2O$, and FeO after reaction) as well as with the Cu *2p*$_{3/2}$ core level spectrum after reaction, that displayed a severe reduction of the component at BE = 934.6 eV ($Cu^{2+}$ hydroxide) and the simultaneous appearance of a new one at BE = 933.7 eV ascribed to $Cu^{2+}$ oxide. Considering the results of XRD analysis, which highlighted the presence of $Cu_2O$ as sole copper oxide phase, it is likely that the XPS peak related to $Cu^{2+}$ oxide is due to a superficial reoxidation of $Cu^+$ exposed to atmospheric conditions within the end of the electrochemical test and the XPS analysis. At the same time, the surface amount of $Cu^+$/Cu(0) (BE = 932.3 eV) increased from 31.3 % to 44.8 % while that of $Cu^{2+}$ decreased from 68.7 % to 55.2 %, indicating that a partial reduction of Cu occurred as well. The spectrum of the Fe *2p* core level of CuMgFe-LDH/FTO after reaction was characterized by the presence of reduced species ($Fe^{2+}$) at BE 710.1 eV (Fe *2p*$_{3/2}$) and 724.1 eV (Fe *2p*$_{1/2}$), which accounted for 19.9 % out for the total Fe.

Overall, the characterization of CuMgFe-LDH/FTO after reaction with several complementary techniques showed that upon photoelectrochemical conditions the layered double hydroxide structure partially decomposed due to the reduction of $Fe^{3+}$ to both $Fe^{2+}$ and metallic iron, as well as the reduction of $Cu^{2+}$ to $Cu^+$.

In literature, it is largely shared and substantiated that the couple $Cu^0/Cu^+$ is the true active site for $CO_2$ activation and reduction [122,123]. Both the LDH samples examined in this work have been found to undergo a partial phase transformation into reduced copper species, which is the reason behind the displayed catalytic performances. However, Fe has been found to promote a larger and tailored copper reduction/phase modification during the reaction, fostering the formation of aggregates of nanoparticles that could in turn be responsible for the superior catalytic activity of CuMgFe-LDH photoelectrode, thanks to the higher exposed active area and/or preferential exposed crystalline planes [124–126]. It has also been suggested that $Fe^0$ itself may act as an active site for $CO_2$ reduction to ethanol [127]. Therefore, beside the better photoelectrocatalytic properties provided by Fe insertion in the CuMg-based LDH (light absorption, conductivity, charge-transfer) iron plays an effective role also in the catalytic process, by promoting catalytic active sites formation thus fostering the formation of less kinetically favoured products as propanol.

Interestingly the prepared catalysts were able to yield products derived from C-C coupling, which is not easy to obtain under $CO_2$ electro- and photoelectroreduction conditions. A mechanistic study has been conducted by Lee et al. [128] on electrocatalytic reduction of carbon dioxide using CuMgAl LDHs displaying a composition analogous to the one used in this work. In the catalytic tests they screened catalyst with low and high copper loadings and showed that increasing the copper content to amounts analogous to what reported here (Cu:Mg:Al 2:1:1) led to the production of $C_{2+}$ products such as ethanol and 1-propanol. They also investigated the reaction mechanism using in situ Raman analysis. They identified that crucial intermediates are adsorbed *CO species, and distinguished between their interaction with the catalyst. They reported that *CO adsorbs with two distinct modes, namely as bridge-adsorbed CO molecules ($CO_{bridge}$), or atop-adsorbed CO molecules ($CO_{atop}$). This different interaction can drive the selectivity toward $C_1$ or $C_{2+}$ products. In fact, they showed that at Cu loadings in the LDH lower than what is used in this study, the $CO_{atop}$ adsorption mode is preferred while both configurations are obtained with a composition analogous to the one used in this work. According to their study the energy barrier for C-C coupling is lower for the $CO_{atop}$–$CO_{bridge}$ couple than for the $CO_{atop}$–$CO_{atop}$ which leads to the production of molecules like ethanol and propanol when using the CuMgAl 2:1:1 composition. The different interaction with the *CO intermediate is provided by the presence of $Cu^0$ / $Cu^+$ species at high Cu loadings which are formed during the reaction as also observed in the characterizations of the used catalyst and that accelerate C-C coupling. The effect of the composition on local pH was also studied showing a higher local pH at higher Cu loadings (CuMgAl 2:1:1), that promotes the C-C coupling and thus the production of $C_{2+}$ products. The reaction mechanism reported is also consistent with what has been observed for the photoelectrocatalytic reduction of $CO_2$ in this work. In addition, the presence of basic sites with high affinity for carbon dioxide [129,130] increases its concentration at the surface and in proximity to copper sites, favouring $C_{2+}$ formation [108,131].

While the observed structural modification has demonstrate to improve the catalytic activity of Cu-based LDH photocathodes to establish that the morphological changes observed in the used catalysts are not decreasing the photoelectrochemical activity, PEC tests were conducted for 24 h at –0.4 V vs RHE on both systems and showed that no significant drop in developed current density was observed, as shown in Figure S11. In details CuMgAl-LDH photocathode exhibited at overall current density of $-0.28 \pm 0.08$ mA cm$^{-2}$ with a decay of 9.01 μA cm$^{-2}$/h while a slightly more variable current density of $-0.9 \pm 0.2$ was observed for CuMgFe-LDH showing a decay of 22.87 μA cm$^{-2}$/h.

A comparative analysis is provided in Table S2 contains literature relevant results in term of $C_{\geq 2}$ products for PEC $CO_2$ reduction. A thorough comparison with literature is not easy due to the employment of different materials, electrodes, cell configurations and reaction conditions which are all parameters affecting performances. Most of the reported works can yield acetic acid or ethanol in small amounts but seldom 1-propanol. Only one other work reports the coproduction of ethanol and propanol but the voltage required is not as low as in this work (-1 V vs RHE compared to –0.4 V vs RHE) [132]. Compared to the other systems for PEC carbon dioxide reduction reported in literature our materials provide innovation being able to provide all the catalytic functions, comprising basic sites for carbon dioxide adsorption close to the copper sites, in a single material easily synthesizable and scalable and showing results which are competitive with more complex catalytic systems.

## 4. Conclusions

The study has demonstrated the potentiality of layered double hydroxides for photoelectrochemical $CO_2$ conversion application. One of the main strategic features of this class of inorganic compounds relies on the compositional variability which can be finely tuned to obtain proper photoelectrochemical properties, catalytic activity, and structural

stability. As demonstrated in this work, incorporation of different metal element such Al or Fe into CuMg-based Layered Double Hydroxides (LDHs) led to different physico-chemical and catalytic behaviour. In detail, CuMgAl-LDH confirmed its interesting properties in $CO_2$RR benefiting of light irradiation to lower the external energy input and showing a better structural stability respect to CuMgFe-LDH. On the other hand, Fe have been found to play a crucial role in boosting photocathode's light-absorption capacity while promoting a tailored reduction of Cu(II) within the LDH structure, leading to the formation of nanoparticle aggregates of $Cu_2O/Cu^0$. The synergistic effect between Fe and Cu in the LDH structure facilitated the creation of active sites essential for the electrocatalytic reduction of $CO_2$, highlighting the importance of Fe in modulating the LDH phase transformation dynamics. The Cu-based LDH photocathodes exhibited good catalytic activity and showed potential for efficient $CO_2$ conversion toward $C_2$ and $C_3$ product such acetic acid, ethanol and 1-propanol. The findings of this research pave the way for further exploration of LDH materials for $CO_2$ conversion and underline the importance of understanding the role of catalyst's elements in optimizing the catalytic properties of LDHs.

## CRediT authorship contribution statement

**Alex Sangiorgi:** Writing – review & editing, Validation, Methodology, Investigation, Data curation, Conceptualization. **Andrea Fasolini:** Writing – review & editing, Writing – original draft, Visualization, Validation, Supervision, Methodology, Investigation, Data curation, Conceptualization. **Nicola Sangiorgi:** Writing – review & editing, Validation, Supervision, Methodology, Investigation, Data curation, Conceptualization. **Eleonora Tosi Brandi:** Writing – review & editing, Writing – original draft, Visualization, Validation, Methodology, Investigation, Data curation, Conceptualization. **Jacopo De Maron:** Writing – review & editing, Writing – original draft, Visualization, Validation, Supervision, Investigation, Data curation, Conceptualization. **Marco Etzi:** Writing – review & editing, Visualization, Validation, Methodology, Investigation, Data curation, Conceptualization. **Erika Scavetta:** Writing – review & editing, Validation, Resources, Project administration, Methodology, Funding acquisition, Conceptualization. **Alessandra Sanson:** Writing – review & editing, Validation, Supervision, Resources, Project administration, Methodology, Funding acquisition, Conceptualization. **Francesco Basile:** Writing – review & editing, Validation, Supervision, Resources, Project administration, Methodology, Funding acquisition, Conceptualization.

## Declaration of Competing Interest

The authors declare that they have no known competing financial interests or personal relationships that could have appeared to influence the work reported in this paper.

## Acknowledgements

Part of this work was financed by the European Union - NextGenerationEU through the Italian Ministry of University and Research under PNRR "Piano Nazionale di Ripresa e Resilienza" - Mission 4 "Istruzione e Ricerca" Component 2 "Dalla ricerca all'impresa", Investment 1.1, "Fondo per il Programma Nazionale di Ricerca e Progetti di Rilevante Interesse Nazionale (PRIN) – Piano Nazionale di Ripresa e Resilienza, addressed to Progetti di Ricerca di Rilevante Interesse Nazionale". D.D. n. 104 del 2/2/2022, Project title: CO2 COnversion to REnewable fuels by dynamic Adsorption and Transformation on LAyered Structured based catalysts - CO2 CORE AT LAST, Codice 2022MPEXJW, CUP J53D23007640006.

This publication has been realized by a researcher (Andrea Fasolini) with aresearch contract co-financed from the European Union – PON Ricerca e Innovazione 2014–2020 ai sensi dell'art. 24, comma 3,lett. a), della Legge 30 dicembre 2010, n. 240 e s.m.i. e del D.M.10 agosto 2021 n. 1062.

Jacopo De Maron acknowledges the National Recovery and Resilience Plan (NRRP), Mission 4 Component 2 Investment 1.3 - Call for tender No. 1561 of 11. 10. 2022 of Ministero dell'Università e della Ricerca (MUR); funded by the European Union – NextGenerationEU, PE0000021, "Network 4 Energy Sustainable Transition – NEST"

## Appendix A. Supporting information

Supplementary data associated with this article can be found in the online version at doi:10.1016/j.apcatb.2025.126276.

## Data availability

Data will be made available on request.

## References

[1] R. Black, K. Cullen, B. Fay, T. Hale, J. Lang, S. Mahmood, S. Smith, 2021, Taking Stock: A global assessment of net zero targets, The Energy & Climate Intelligence Unit & Oxford Net Zero, https://eciu.net/analysis/reports/2021/taking-stock-assessment-net-zero-targets..

[2] J.L. White, M.F. Baruch, J.E. Pander, Y. Hu, I.C. Fortmeyer, J.E. Park, T. Zhang, K. Liao, J. Gu, Y. Yan, T.W. Shaw, E. Abelev, A.B. Bocarsly, Light-driven heterogeneous reduction of carbon dioxide: photocatalysts and photoelectrodes, Chem. Rev. 115 (2015) 12888–12935, https://doi.org/10.1021/acs.chemrev.5b00370.

[3] E. Kalamaras, M.M. Maroto-Valer, M. Shao, J. Xuan, H. Wang, Solar carbon fuel via photoelectrochemistry, Catal. Today 317 (2018) 56–75, https://doi.org/10.1016/j.cattod.2018.02.045.

[4] V. Kumaravel, J. Bartlett, S.C. Pillai, Photoelectrochemical conversion of carbon dioxide (CO $_2$) into fuels and value-added products, ACS Energy Lett. 5 (2020) 486–519, https://doi.org/10.1021/acsenergylett.9b02585.

[5] B. Tang, F.-X. Xiao, An overview of solar-driven photoelectrochemical CO2 conversion to chemical fuels, ACS Catal. 12 (2022) 9023–9057, https://doi.org/10.1021/acscatal.2c01667.

[6] K. Xu, Q. Zhang, X. Zhou, M. Zhu, H. Chen, Recent progress and perspectives on photocathode materials for CO2 catalytic reduction, Nanomaterials 13 (2023) 1683, https://doi.org/10.3390/nano13101683.

[7] L. Wan, R. Chen, D.W.Fung Cheung, L. Wu, J. Luo, Solar driven CO 2 reduction: from materials to devices, J. Mater. Chem. A 11 (2023) 12499–12520, https://doi.org/10.1039/D3TA00267E.

[8] Y. Hori, H. Wakebe, T. Tsukamoto, O. Koga, Electrocatalytic process of CO selectivity in electrochemical reduction of CO2 at metal electrodes in aqueous media, Electrochim. Acta 39 (1994) 1833–1839, https://doi.org/10.1016/0013-4686(94)85172-7.

[9] A. Bagger, W. Ju, A.S. Varela, P. Strasser, J. Rossmeisl, Electrochemical CO2 reduction: a classification problem, ChemPhysChem 18 (2017) 3266–3273, https://doi.org/10.1002/cphc.201700736.

[10] D.H. Won, C.H. Choi, J. Chung, S.I. Woo, Photoelectrochemical production of formic acid and methanol from carbon dioxide on metal-decorated CuO/Cu2O-layered thin films under visible light irradiation, Appl. Catal. B Environ. 158159 (2014) 217–223, https://doi.org/10.1016/j.apcatb.2014.04.021.

[11] H. Homayoni, W. Chanmanee, N.R. de Tacconi, B.H. Dennis, K. Rajeshwar, Continuous flow photoelectrochemical reactor for solar conversion of carbon dioxide to alcohols, J. Electrochem. Soc. 162 (2015) E115, https://doi.org/10.1149/2.0331508jes.

[12] H.-Y. Kang, D.-H. Nam, K.D. Yang, W. Joo, H. Kwak, H.-H. Kim, S.-H. Hong, K. T. Nam, Y.-C. Joo, Synthetic mechanism discovery of monophase cuprous oxide for record high photoelectrochemical conversion of CO2 to methanol in water, ACS Nano 12 (2018) 8187–8196, https://doi.org/10.1021/acsnano.8b03293.

[13] M. Xia, L. Pan, Y. Liu, J. Gao, J. Li, M. Mensi, K. Sivula, S.M. Zakeeruddin, D. Ren, M. Grätzel, Efficient Cu2O photocathodes for aqueous photoelectrochemical CO2 reduction to formate and syngas, J. Am. Chem. Soc. 145 (2023) 27939–27949, https://doi.org/10.1021/jacs.3c06146.

[14] K. Wang, Y. Ma, Y. Liu, W. Qiu, Q. Wang, X. Yang, M. Liu, X. Qiu, W. Li, J. Li, Insights into the development of Cu-based photocathodes for carbon dioxide (CO $_2$) conversion, Green. Chem. 23 (2021) 3207–3240, https://doi.org/10.1039/D0GC04417B.

[15] M.A. Lumley, A. Radmilovic, Y.J. Jang, A.E. Lindberg, K.-S. Choi, Perspectives on the development of oxide-based photocathodes for solar fuel production, J. Am. Chem. Soc. 141 (2019) 18358–18369, https://doi.org/10.1021/jacs.9b07976.

[16] H. Liang, M. Li, Z. Li, W. Xie, T. Zhang, Q. Wang, Photoelectrochemical CO2 reduction with copper-based photocathodes, J. CO2 Util. 79 (2024) 102639, https://doi.org/10.1016/j.jcou.2023.102639.

[17] K.M. Rezaul Karim, H.R. Ong, H. Abdullah, A. Yousuf, C.K. Cheng, M.M. Rahman Khan, Photoelectrochemical reduction of carbon dioxide to methanol on p-type CuFe2O4 under visible light irradiation, Int. J. Hydrog. Energy 43 (2018) 18185–18193, https://doi.org/10.1016/j.ijhydene.2018.07.174.

[18] J. Yuan, C. Gu, W. Ding, C. Hao, Photo-electrochemical reduction of carbon dioxide into methanol at CuFeO $_2$ nanoparticle-decorated CuInS $_2$ thin-film

photocathodes, Energy Fuels 34 (2020) 9914–9922, https://doi.org/10.1021/acs.energyfuels.0c02009.
[19] J. Gu, A. Wuttig, J.W. Krizan, Y. Hu, Z.M. Detweiler, R.J. Cava, A.B. Bocarsly, Mg-doped CuFeO $_2$ photocathodes for photoelectrochemical reduction of carbon dioxide, J. Phys. Chem. C. 117 (2013) 12415–12422, https://doi.org/10.1021/jp402007z.
[20] X. Yang, E.A. Fugate, Y. Mueanngern, L.R. Baker, Photoelectrochemical CO $_2$ reduction to acetate on iron–copper oxide catalysts, ACS Catal. 7 (2017) 177–180, https://doi.org/10.1021/acscatal.6b02984.
[21] V. Rives, Layered Double Hydroxides: Present and Future, Nova Science Publishers, 2001. ⟨https://books.google.it/books?id=U5c5zzqjthgC⟩.
[22] N. Dewangan, W.M. Hui, S. Jayaprakash, A.-R. Bawah, A.J. Poerjoto, T. Jie, A. Jangam, K. Hidajat, S. Kawi, Recent progress on layered double hydroxide (LDH) derived metal-based catalysts for CO2 conversion to valuable chemicals, Catal. Today 356 (2020) 490–513, https://doi.org/10.1016/j.cattod.2020.06.020.
[23] D. Chaillot, S. Bennici, J. Brendlé, Layered double hydroxides and LDH-derived materials in chosen environmental applications: a review, Environ. Sci. Pollut. Res 28 (2021) 24375–24405, https://doi.org/10.1007/s11356-020-08498-6.
[24] Y. Ren, Y. Yang, L. Chen, L. Wang, Y. Shi, P. Yin, W. Wang, M. Shao, X. Zhang, M. Wei, Synergetic effect of Cu0 −Cu+ derived from layered double hydroxides toward catalytic transfer hydrogenation reaction, Appl. Catal. B Environ. 314 (2022) 121515, https://doi.org/10.1016/j.apcatb.2022.121515.
[25] Z.-H. Zhang, Z. Sun, T.-Q. Yuan, Recent advances in the catalytic upgrading of biomass platform chemicals via hydrotalcite-derived metal catalysts, Trans. Tianjin Univ. 28 (2022) 89–111, https://doi.org/10.1007/s12209-021-00307-6.
[26] R.M. de Lima Rodrigues, C.B. Reis, J.-G. Eon, L.A. Palacio, Oxidative dehydrogenation of propane using Ni–Mg–Al mixed oxide catalysts from hydrotalcite-type precursors, Braz. J. Chem. Eng. 40 (2023) 1055–1065, https://doi.org/10.1007/s43153-022-00295-7.
[27] E. Orfei, A. Fasolini, S. Abate, N. Dimitratos, F. Basile, Layered-double hydroxides and derived oxide as CRM-free highly active catalysts for the reduction of 4-nitrophenol, Catal. Today 419 (2023) 114153, https://doi.org/10.1016/j.cattod.2023.114153.
[28] P. Benito, G. Fornasari, F. Basile, T. Tabanelli, C. Lucarelli, A. Fasolini, N. Dimitratos, S. Albonetti, F. Cavani, F. Trifirò, The several hydrotalcites investigated as precursors of catalysts by Angelo Vaccari, Catal. Today 439 (2024) 114791, https://doi.org/10.1016/j.cattod.2024.114791.
[29] D. Tonelli, E. Scavetta, M. Giorgetti, Layered-double-hydroxide-modified electrodes: electroanalytical applications, Anal. Bioanal. Chem. 405 (2013) 603–614, https://doi.org/10.1007/s00216-012-6586-2.
[30] N. Baig, M. Sajid, Applications of layered double hydroxides based electrochemical sensors for determination of environmental pollutants: a review, Trends Environ. Anal. Chem. 16 (2017) 1–15, https://doi.org/10.1016/j.teac.2017.10.003.
[31] I. Gualandi, M. Tessarolo, F. Mariani, D. Arcangeli, L. Possanzini, D. Tonelli, B. Fraboni, E. Scavetta, Layered double hydroxide-modified organic electrochemical transistor for glucose and lactate biosensing, Sensors 20 (2020) 3453, https://doi.org/10.3390/s20123453.
[32] D. Tonelli, I. Gualandi, E. Musella, E. Scavetta, Synthesis and characterization of layered double hydroxides as materials for electrocatalytic applications, Nanomaterials 11 (2021) 725, https://doi.org/10.3390/nano11030725.
[33] C. Mousty, H. Farhat, Recent advances in layered double hydroxides-based electrochemical sensors: insight in transition metal contribution, Electroanalysis 35 (2023) e202200527, https://doi.org/10.1002/elan.202200527.
[34] V.K. Ameena Shirin, R. Sankar, A.P. Johnson, H.V. Gangadharappa, K. Pramod, Advanced drug delivery applications of layered double hydroxide, J. Control. Release 330 (2021) 398–426, https://doi.org/10.1016/j.jconrel.2020.12.041.
[35] A.L.M.D. de Sousa, W.M. dos Santos, M.L. de Souza, L.C.P.B.B. Silva, A.E.H. K. Yun, C.S.B. Aguilera, B. de, F. Chagas, L.A. Rolim, R.M.F. da Silva, P.J.R. Neto, Layered double hydroxides as promising excipients for drug delivery purposes, Eur. J. Pharm. Sci. 165 (2021) 105922, https://doi.org/10.1016/j.ejps.2021.105922.
[36] T. Kameda, H. Takeuchi, T. Yoshioka, Uptake of heavy metal ions from aqueous solution using Mg–Al layered double hydroxides intercalated with citrate, malate, and tartrate, Sep. Purif. Technol. 62 (2008) 330–336, https://doi.org/10.1016/j.seppur.2008.02.001.
[37] L. Santamaría, M.A. Vicente, S.A. Korili, A. Gil, Progress in the removal of pharmaceutical compounds from aqueous solution using layered double hydroxides as adsorbents: a review, J. Environ. Chem. Eng. 8 (2020) 104577, https://doi.org/10.1016/j.jece.2020.104577.
[38] M.A. Ahmed, A.A. Mohamed, A systematic review of layered double hydroxide-based materials for environmental remediation of heavy metals and dye pollutants, Inorg. Chem. Commun. 148 (2023) 110325, https://doi.org/10.1016/j.inoche.2022.110325.
[39] W. Shi, Y. Lin, S. Zhang, R. Tian, R. Liang, M. Wei, D.G. Evans, X. Duan, Study on UV-shielding mechanism of layered double hydroxide materials, Phys. Chem. Chem. Phys. 15 (2013) 18217–18222, https://doi.org/10.1039/C3CP52819G.
[40] Z.M. Mir, A. Bastos, D. Höche, M.L. Zheludkevich, Recent advances on the application of layered double hydroxides in concrete—A review, Materials 13 (2020) 1426, https://doi.org/10.3390/ma13061426.
[41] A. Fasolini, S. Abate, D. Barbera, G. Centi, F. Basile, Pure H2 production by methane oxy-reforming over Rh-Mg-Al hydrotalcite-derived catalysts coupled with a Pd membrane, Appl. Catal. A Gen. 581 (2019) 91–102, https://doi.org/10.1016/j.apcata.2019.05.024.
[42] H.L. Huynh, Z. Yu, CO2 methanation on hydrotalcite-derived catalysts and structured reactors: a review, Energy Technol. 8 (2020) 1901475, https://doi.org/10.1002/ente.201901475.
[43] P.H. Ho, F. Ospitali, G.S. De Luna, G. Fornasari, A. Vaccari, P. Benito, Electrodeposition of Rh/Mg/Al hydroxides with different Mg-contents on metallic foams as catalyst precursors, Appl. Clay Sci. 191 (2020) 105599, https://doi.org/10.1016/j.clay.2020.105599.
[44] P.H. Ho, G. Sanghez de Luna, F. Ospitali, G. Fornasari, A. Vaccari, P. Benito, Open-cell foams coated by Ni/X/Al hydrotalcite-type derived catalysts (X = Ce, La, Y) for CO2 methanation, J. CO2 Util. 42 (2020) 101327, https://doi.org/10.1016/j.jcou.2020.101327.
[45] P.H. Ho, F. Ospitali, G. Sanghez de Luna, G. Fornasari, A. Vaccari, P. Benito, Coating of Rh/Mg/Al hydrotalcite-like materials on FeCrAl fibers by electrodeposition and application for syngas production, Energy Technol. 8 (2020) 1901018, https://doi.org/10.1002/ente.201901018.
[46] N. Schiaroli, C. Lucarelli, M.C. Iapalucci, G. Fornasari, A. Crimaldi, A. Vaccari, Combined reforming of clean biogas over nanosized Ni–Rh bimetallic clusters, Catalysts 10 (2020) 1345, https://doi.org/10.3390/catal10111345.
[47] P.H. Ho, G. Sanghez de Luna, N. Schiaroli, A. Natoli, F. Ospitali, M. Battisti, F. di Renzo, C. Lucarelli, A. Vaccari, G. Fornasari, P. Benito, Effect of Fe and La on the performance of NiMgAl HT-derived catalysts in the methanation of CO2 and biogas, Ind. Eng. Chem. Res. 61 (2022) 10511–10521, https://doi.org/10.1021/acs.iecr.2c00687.
[48] P. Tarifa, N. Schiaroli, P.H. Ho, F. Cañaza, F. Ospitali, G. Sanghez de Luna, C. Lucarelli, G. Fornasari, A. Vaccari, A. Monzon, P. Benito, Steam reforming of clean biogas over Rh and Ru open-cell metallic foam structured catalysts, Catal. Today 383 (2022) 74–83, https://doi.org/10.1016/j.cattod.2021.03.024.
[49] A. Fasolini, E. Spennati, S. Ebrahim Atakoohi, M. Percivale, G. Busca, F. Basile, G. Garbarino, A study of CO2 hydrogenation over Ni-MgAlOx catalysts derived from hydrotalcite precursors, Catal. Today 423 (2023) 114271, https://doi.org/10.1016/j.cattod.2023.114271.
[50] A. Misol, I. Giarnieri, F. Ospitali, A. Ballarini, J. Jiménez-Jiménez, E. Rodríguez-Castellón, F.M. Labajos, G. Fornasari, P. Benito, CO2 hydrogenation over Ru hydrotalcite-derived catalysts, Catal. Today 425 (2024) 114362, https://doi.org/10.1016/j.cattod.2023.114362.
[51] F. Cavani, F. Trifirò, A. Vaccari, Hydrotalcite-type anionic clays: preparation, properties and applications, Catal. Today 11 (1991) 173–301, https://doi.org/10.1016/0920-5861(91)80068-K.
[52] Y. Vlamidis, E. Scavetta, M. Gazzano, D. Tonelli, Iron vs aluminum based layered double hydroxides as water splitting catalysts, Electrochim. Acta 188 (2016) 653–660, https://doi.org/10.1016/j.electacta.2015.12.059.
[53] Y. Wang, D. Yan, S. El Hankari, Y. Zou, S. Wang, Recent progress on layered double hydroxides and their derivatives for electrocatalytic water splitting, Adv. Sci. 5 (2018) 1800064, https://doi.org/10.1002/advs.201800064.
[54] E. Musella, I. Gualandi, E. Scavetta, M. Gazzano, A. Rivalta, E. Venuti, M. Christian, V. Morandi, D. Tonelli, Electrochemical approach for the production of layered double hydroxides with a well-defined Co/MeIII ratio, Chem. A Eur. J. 25 (2019) 16301–16310, https://doi.org/10.1002/chem.201903288.
[55] M. Shao, F. Ning, J. Zhao, M. Wei, D.G. Evans, X. Duan, Hierarchical layered double hydroxide microspheres with largely enhanced performance for ethanol electrooxidation, Adv. Funct. Mater. 23 (2013) 3513–3518, https://doi.org/10.1002/adfm.201202825.
[56] E. Musella, I. Gualandi, E. Scavetta, A. Rivalta, E. Venuti, M. Christian, V. Morandi, A. Mullaliu, M. Giorgetti, D. Tonelli, Newly developed electrochemical synthesis of Co-based layered double hydroxides: toward noble metal-free electro-catalysis, J. Mater. Chem. A 7 (2019) 11241–11249, https://doi.org/10.1039/C8TA11812D.
[57] Y. Song, Z. Li, K. Fan, Z. Ren, W. Xie, Y. Yang, M. Shao, M. Wei, Ultrathin layered double hydroxides nanosheets array towards efficient electrooxidation of 5-hydroxymethylfurfural coupled with hydrogen generation, Appl. Catal. B Environ. 299 (2021) 120669, https://doi.org/10.1016/j.apcatb.2021.120669.
[58] J.Y. Wang, L.P. Sun, Q. Li, L.H. Huo, H. Zhao, Energy-efficient hydrogen production coupled with methanol oxidation using NiFe LDH@NiMo alloy heterostructure, Mater. Today Chem. 27 (2023) 101338, https://doi.org/10.1016/j.mtchem.2022.101338.
[59] L. Li, J. Yang, L. Li, Y. Huang, J. Zhao, Electrolytic reduction of CO2 in KHCO3 and alkanolamine solutions with layered double hydroxides intercalated with gold or copper, Electrochim. Acta 402 (2022) 139523, https://doi.org/10.1016/j.electacta.2021.139523.
[60] K. Iwase, T. Hirano, I. Honma, Copper aluminum layered double hydroxides with different compositions and morphologies as electrocatalysts for the carbon dioxide reduction reaction, ChemSusChem 15 (2022) e202102340, https://doi.org/10.1002/cssc.202102340.
[61] J. Zhang, X. Mao, B. Pan, J. Xu, X. Ding, N. Han, L. Wang, Y. Wang, Y. Li, Surface promotion of copper nanoparticles with alumina clusters derived from layered double hydroxide accelerates CO2 reduction to ethylene in membrane electrode assemblies, Nano Res. 16 (2023) 4685–4690, https://doi.org/10.1007/s12274-022-5128-2.
[62] M. Serafini, F. Mariani, A. Fasolini, E.T. Brandi, E. Scavetta, F. Basile, D. Tonelli, Electrosynthesized CuMgAl layered double hydroxides as new catalysts for the electrochemical reduction of CO $_2$, Adv. Funct. Mater. (2023) 2300345, https://doi.org/10.1002/adfm.202300345.
[63] S. Xia, L. Zhang, X. Zhou, G. Pan, Z. Ni, The photocatalytic property for water splitting and the structural stability of CuMgM layered double hydroxides (M=Al, Cr, Fe, Ce), Appl. Clay Sci. 114 (2015) 577–585, https://doi.org/10.1016/j.clay.2015.06.023.

[64] S. Nayak, K. Parida, Plethora of preparatory features on single layered double hydroxide towards energy conversion process, Mater. Res. Bull. 162 (2023) 112185, https://doi.org/10.1016/j.materresbull.2023.112185.

[65] H. Boumeriame, E.S. Da Silva, A.S. Cherevan, T. Chafik, J.L. Faria, D. Eder, Layered double hydroxide (LDH)-based materials: a mini-review on strategies to improve the performance for photocatalytic water splitting, J. Energy Chem. 64 (2022) 406–431, https://doi.org/10.1016/j.jechem.2021.04.050.

[66] N. Ahmed, Y. Shibata, T. Taniguchi, Y. Izumi, Photocatalytic conversion of carbon dioxide into methanol using zinc–copper–M(III) (M=aluminum, gallium) layered double hydroxides, J. Catal. 279 (2011) 123–135, https://doi.org/10.1016/j.jcat.2011.01.004.

[67] C. Prasad, H. Tang, Q.Q. Liu, S. Zulfiqar, S. Shah, I. Bahadur, An overview of semiconductors/layered double hydroxides composites: properties, synthesis, photocatalytic and photoelectrochemical applications, J. Mol. Liq. 289 (2019) 111114, https://doi.org/10.1016/j.molliq.2019.111114.

[68] X. Xiong, Y. Zhao, R. Shi, W. Yin, Y. Zhao, G.I.N. Waterhouse, T. Zhang, Selective photocatalytic CO2 reduction over Zn-based layered double hydroxides containing tri or tetravalent metals, Sci. Bull. 65 (2020) 987–994, https://doi.org/10.1016/j.scib.2020.03.032.

[69] G. Ding, C. Li, Y. Ni, L. Chen, L. Shuai, G. Liao, Layered double hydroxides and their composites as high-performance photocatalysts for CO 2 reduction, EES Catal. 1 (2023) 369–391, https://doi.org/10.1039/D3EY00080J.

[70] H. Qi, J. Wolfe, D. Fichou, Z. Chen, Cu2O photocathode for low bias photoelectrochemical water splitting enabled by NiFe-layered double hydroxide Co-catalyst, Sci. Rep. 6 (2016) 30882, https://doi.org/10.1038/srep30882.

[71] M. Arif, G. Yasin, M. Shakeel, M.Asim Mushtaq, W. Ye, X. Fang, S. Ji, D. Yan, Hierarchical CoFe-layered double hydroxide and g-C 3 N 4 heterostructures with enhanced bifunctional photo/electrocatalytic activity towards overall water splitting, Mater. Chem. Front. 3 (2019) 520–531, https://doi.org/10.1039/C8QM00677F.

[72] A. Pirkarami, S. Rasouli, E. Ghasemi, 3-D CdS@NiCo layered double hydroxide core-shell photoelectrocatalyst used for efficient overall water splitting, Appl. Catal. B Environ. 241 (2019) 28–40, https://doi.org/10.1016/j.apcatb.2018.09.021.

[73] R. Gao, J. Zhu, D. Yan, Transition metal-based layered double hydroxides for photo(electro)chemical water splitting: a mini review, Nanoscale 13 (2021) 13593–13603, https://doi.org/10.1039/D1NR03409J.

[74] P. Wei, Y. Wen, K. Lin, X. Li, Turning off the “shunt channel” by coating with CoFe layered double hydroxide nanocrystals for efficient photoelectrocatalytic water splitting, Inorg. Chem. Front. 9 (2022) 4685–4694, https://doi.org/10.1039/D2QI00760F.

[75] W. Bao, Y. Tang, J. Yu, W. Yan, C. Wang, Y. Li, Z. Wang, J. Yang, L. Zhang, F. Yu, Si-doped ZnAl-LDH nanosheets by layer-engineering for efficient photoelectrocatalytic water splitting, Appl. Catal. B Environ. Energy 346 (2024) 123706, https://doi.org/10.1016/j.apcatb.2024.123706.

[76] J.H. Lee, J. Chang, J.-H. Cha, D.-Y. Jung, S.S. Kim, J.M. Kim, Anthraquinone sulfonate modified, layered double hydroxide nanosheets for dye-sensitized solar cells, Chem. A Eur. J. 16 (2010) 8296–8299, https://doi.org/10.1002/chem.201000703.

[77] S. Naseem, B.R. Gevers, F.J.W.J. Labuschagné, A. Leuteritz, Preparation of photoactive transition-metal layered double hydroxides (LDH) to replace dye-sensitized materials in solar cells, Materials 13 (2020), https://doi.org/10.3390/ma13194384.

[78] A. Fasolini, N. Sangiorgi, E.T. Brandi, A. Sangiorgi, F. Mariani, E. Scavetta, A. Sanson, F. Basile, Increased efficiency and stability of dye-sensitized solar cells (DSSC) photoanode by intercalation of Eosin Y into Zn/Al layered double hydroxide, Appl. Clay Sci. 212 (2021) 106219, https://doi.org/10.1016/j.clay.2021.106219.

[79] X. Liu, S. Tao, J. Zhang, Y. Zhu, R. Ma, J. Lu, Ultrathin p–n type $Cu_2$ O/CuCoCr-layered double hydroxide heterojunction nanosheets for photo-assisted aqueous Zn–$CO_2$ batteries, J. Mater. Chem. A 9 (2021) 26061–26068, https://doi.org/10.1039/D1TA07522E.

[80] F. Loprete, E. Tosi Brandi, F. Calcagno, J. De Maron, A. Fasolini, R. Tarroni, F. Basile, I. Rivalta, Advancing $CO_2$ conversion with Cu-LDHs: a review of computational and experimental studies, Chem. Rec. (2025), https://doi.org/10.1002/tcr.202500014.

[81] C.A. Castro, A. Centeno, S.A. Giraldo, Iron promotion of the TiO2 photosensitization process towards the photocatalytic oxidation of azo dyes under solar-simulated light irradiation, Mater. Chem. Phys. 129 (2011) 1176–1183, https://doi.org/10.1016/j.matchemphys.2011.05.082.

[82] S. Casadio, A. Gondolini, N. Sangiorgi, A. Candini, A. Sanson, Highly transparent Bi 4 Ti 3 O 12 thin-film electrodes for ferroelectric-enhanced photoelectrochemical processes, Sustain. Energy Fuels 7 (2023) 1107–1118, https://doi.org/10.1039/D2SE01372J.

[83] S.-M. Xu, T. Pan, Y.-B. Dou, H. Yan, S.-T. Zhang, F.-Y. Ning, W.-Y. Shi, M. Wei, Theoretical and experimental study on MIIMIII-layered double hydroxides as efficient photocatalysts toward oxygen evolution from water, J. Phys. Chem. C. 119 (2015) 18823–18834, https://doi.org/10.1021/acs.jpcc.5b01819.

[84] S.-M. Xu, H. Yan, M. Wei, Band structure engineering of transition-metal-based layered double hydroxides toward photocatalytic oxygen evolution from water: a theoretical–experimental combination study, J. Phys. Chem. C. 121 (2017) 2683–2695, https://doi.org/10.1021/acs.jpcc.6b10159.

[85] S. Iguchi, S. Kikkawa, K. Teramura, S. Hosokawa, T. Tanaka, Investigation of the electrochemical and photoelectrochemical properties of Ni–Al LDH photocatalysts, Phys. Chem. Chem. Phys. 18 (2016) 13811–13819, https://doi.org/10.1039/C6CP01646D.

[86] P.P. Sahoo, B. Zoellner, P.A. Maggard, Optical, electronic, and photoelectrochemical properties of the p-type $Cu_{3-x}VO_4$ semiconductor, J. Mater. Chem. A 3 (2015) 4501–4509, https://doi.org/10.1039/C4TA04876H.

[87] C.C.L. McCrory, S. Jung, J.C. Peters, T.F. Jaramillo, Benchmarking heterogeneous electrocatalysts for the oxygen evolution reaction, J. Am. Chem. Soc. 135 (2013) 16977–16987, https://doi.org/10.1021/ja407115p.

[88] A. Lamberti, A. Sacco, S. Bianco, M. Quaglio, D. Manfredi, C.F. Pirri, Enhancement of electron lifetime in dye-sensitized solar cells using anodically grown TiO2 nanotube/nanoparticle composite photoanodes, Microelectron. Eng. 111 (2013) 137–142, https://doi.org/10.1016/j.mee.2013.03.037.

[89] F. Fabregat-Santiago, J. Bisquert, G. Garcia-Belmonte, G. Boschloo, A. Hagfeldt, Influence of electrolyte in transport and recombination in dye-sensitized solar cells studied by impedance spectroscopy, Sol. Energy Mater. Sol. Cells 87 (2005) 117–131, https://doi.org/10.1016/j.solmat.2004.07.017.

[90] Z. Xu, B. Hou, F. Zhao, S. Suo, Y. Liu, H. Shi, Z. Cai, C.L. Hill, D.G. Musaev, M. Mecklenburg, S.B. Cronin, T. Lian, Direct *In Situ* measurement of quantum efficiencies of charge separation and proton reduction at $TiO_2$ -protected GaP photocathodes, J. Am. Chem. Soc. 145 (2023) 2860–2869, https://doi.org/10.1021/jacs.2c10578.

[91] D. Li, Y. Cai, Y. Ding, R. Li, M. Lu, L. Jiang, Layered double hydroxides as precursors of Cu catalysts for hydrogen production by water-gas shift reaction, Int. J. Hydrog. Energy 40 (2015) 10016–10025, https://doi.org/10.1016/j.ijhydene.2015.05.183.

[92] L. Wu, B. Peng, Q. Li, Q. Wang, X. Yan, K. Li, Q. Lin, Effects of Cu 2+ incorporation on ZnAl-layered double hydroxide, N. J. Chem. 44 (2020) 5293–5302, https://doi.org/10.1039/D0NJ00278J.

[93] K. Parida, M. Satpathy, L. Mohapatra, Incorporation of Fe3+ into Mg/Al layered double hydroxide framework: effects on textural properties and photocatalytic activity for H2 generation, J. Mater. Chem. 22 (2012) 7350, https://doi.org/10.1039/c2jm15658j.

[94] M. Gazzano, W. Kagunya, D. Matteuzzi, A. Vaccari, Neutron diffraction studies of polycrystalline Ni/Mg/Al mixed oxides obtained from hydrotalcite-like precursors, J. Phys. Chem. B 101 (1997) 4514–4519, https://doi.org/10.1021/jp963761q.

[95] Y. Sakai, T. Kakuda, T. Futakuchi, M. Adachi, Preparation of (Ba,Sr)$TiO_3$ thick films with Ni electrodes by screen printing, Jpn. J. Appl. Phys. 49 (2010) 09MA12, https://doi.org/10.1143/JJAP.49.09MA12.

[96] Y. Sakai, T. Karaki, Preparation of Pb($Mg_{1/3}Nb_{2/3}$)$TiO_3$ –$PbTiO_3$ thick films with highly preferred orientation via screen printing, Jpn. J. Appl. Phys. 62 (SM) (2023) 1004, https://doi.org/10.35848/1347-4065/ace36c.

[97] N.S. McIntyre, M.G. Cook, X-ray photoelectron studies on some oxides and hydroxides of cobalt, nickel, and copper, Anal. Chem. 47 (1975) 2208–2213, https://doi.org/10.1021/ac60363a034.

[98] M.C. Biesinger, Advanced analysis of copper X-ray photoelectron spectra, Surf. Interface Anal. 49 (2017) 1325–1334, https://doi.org/10.1002/sia.6239.

[99] M.E.C. Pascuzzi, A.J.W. Man, A. Goryachev, J.P. Hofmann, E.J.M. Hensen, Investigation of the stability of NiFe-(oxy)hydroxide anodes in alkaline water electrolysis under industrially relevant conditions, Catal. Sci. Technol. 10 (2020) 5593–5601, https://doi.org/10.1039/D0CY01179G.

[100] J. Stoch, J. Gablankowska-Kukucz, The effect of carbonate contaminations on the XPS O 1s band structure in metal oxides, Surf. Interface Anal. 17 (1991) 165–167, https://doi.org/10.1002/sia.740170308.

[101] M.C. Biesinger, L.W.M. Lau, A.R. Gerson, R.St.C. Smart, Resolving surface chemical states in XPS analysis of first row transition metals, oxides and hydroxides: Sc, Ti, V, Cu and Zn, Appl. Surf. Sci. 257 (2010) 887–898, https://doi.org/10.1016/j.apsusc.2010.07.086.

[102] W.M. Skinner, C.A. Prestidge, R.St.C. Smart, Irradiation effects during XPS studies of Cu(II) activation of zinc sulphide, Surf. Interface Anal. 24 (1996) 620–626, https://doi.org/10.1002/(SICI)1096-9918(19960916)24:9%253C620::AID-SIA151%253E3.0.CO;2-Y.

[103] C. Roy, B. Sebok, S.B. Scott, E.M. Fiordaliso, J.E. Sørensen, A. Bodin, D. B. Trimarco, C.D. Damsgaard, P.C.K. Vesborg, O. Hansen, I.E.L. Stephens, J. Kibsgaard, I. Chorkendorff, Impact of nanoparticle size and lattice oxygen on water oxidation on NiFeOxHy, Nat. Catal. 1 (2018) 820–829, https://doi.org/10.1038/s41929-018-0162-x.

[104] M. Etzi Coller Pascuzzi, E. Selinger, A. Sacco, M. Castellino, P. Rivolo, S. Hernández, G. Lopinski, I. Tamblyn, R. Nasi, S. Esposito, M. Manzoli, B. Bonelli, M. Armandi, Beneficial effect of Fe addition on the catalytic activity of electrodeposited MnOx films in the water oxidation reaction, Electrochim. Acta 284 (2018) 294–302, https://doi.org/10.1016/j.electacta.2018.07.148.

[105] A.W. Bott, K. Avenue, Current separations, Electrochem. Semicond. (1998).

[106] Q. Lu, J. Rosen, Y. Zhou, G.S. Hutchings, Y.C. Kimmel, J.G. Chen, F. Jiao, A selective and efficient electrocatalyst for carbon dioxide reduction, Nat. Commun. 5 (2014) 3242, https://doi.org/10.1038/ncomms4242.

[107] W. Deng, P. Zhang, B. Seger, J. Gong, Unraveling the rate-limiting step of two-electron transfer electrochemical reduction of carbon dioxide, Nat. Commun. 13 (2022) 803, https://doi.org/10.1038/s41467-022-28436-z.

[108] M. Serafini, F. Mariani, A. Fasolini, E. Scavetta, F. Basile, D. Tonelli, Nanostructured copper-based electrodes electrochemically synthesized on a carbonaceous gas diffusion membrane with catalytic activity for the electroreduction of CO2, ACS Appl. Mater. Interfaces 13 (2021) 57451–57461, https://doi.org/10.1021/acsami.1c18844.

[109] E.M.S. Elfeky, M.R. Shehata, Y.H. Elbashar, M.H. Barakat, W.M.A.E. Rouby, Developing the sensing features of copper electrodes as an environmental friendly detection tool for chemical oxygen demand, RSC Adv. 12 (2022) 4199–4208, https://doi.org/10.1039/D1RA09411D.

[110] K. Nejati, K. Asadpour-Zeynali, Electrochemical synthesis of nickel–iron layered double hydroxide: application as a novel modified electrode in electrocatalytic reduction of metronidazole, Mater. Sci. Eng. C 35 (2014) 179–184, https://doi.org/10.1016/j.msec.2013.11.003.
[111] K. Duschek, M. Uhlemann, H. Schlörb, K. Nielsch, K. Leistner, Electrochemical and in situ magnetic study of iron/iron oxide films oxidized and reduced in KOH solution for magneto-ionic switching, Electrochem. Commun. 72 (2016) 153–156, https://doi.org/10.1016/j.elecom.2016.09.018.
[112] Q. Ding, F. Meng, C.R. English, M. Cabán-Acevedo, M.J. Shearer, D. Liang, A. S. Daniel, R.J. Hamers, S. Jin, Efficient photoelectrochemical hydrogen generation using heterostructures of Si and chemically exfoliated metallic MoS2, J. Am. Chem. Soc. 136 (2014) 8504–8507, https://doi.org/10.1021/ja5025673.
[113] S.F. Lee, E. Jimenez-Relinque, I. Martinez, M. Castellote, Photoelectrochemical global approach to the behaviour of nanostructured anatase under different irradiation conditions, Catal. Today 397399 (2022) 286–295, https://doi.org/10.1016/j.cattod.2021.09.006.
[114] S. Anantharaj, S. Noda, Appropriate use of electrochemical impedance spectroscopy in water splitting electrocatalysis, ChemElectroChem 7 (2020) 2297–2308, https://doi.org/10.1002/celc.202000515.
[115] A.R.C. Bredar, A.L. Chown, A.R. Burton, B.H. Farnum, Electrochemical impedance spectroscopy of metal oxide electrodes for energy applications, ACS Appl. Energy Mater. 3 (2020) 66–98, https://doi.org/10.1021/acsaem.9b01965.
[116] G. She, J. Ma, X. Hao, C. Ru, H. Zhang, L. Mu, X. Qi, W. Shi, Strategies for reducing the overpotential of one-dimensional Si nanostructured photoelectrodes for solar hydrogen production, EES Catal. 1 (2023) 392–412, https://doi.org/10.1039/D3EY00073G.
[117] Y. Hori, K. Kikuchi, S. Suzuki, Production of CO AND CH4 in electrochemical reduction of CO2 at metal electrodes in aqueous hydrogencarbonate solution, Chem. Lett. 14 (1985) 1695–1698, https://doi.org/10.1246/cl.1985.1695.
[118] Y. Hori, Electrochemical CO2 Reduction on Metal Electrodes, in: C.G. Vayenas, R. E. White, M.E. Gamboa-Aldeco (Eds.), Modern Aspects of Electrochemistry, Springer, New York, NY, 2008, pp. 89–189, https://doi.org/10.1007/978-0-387-49489-0_3.
[119] W. Yuan, Y. Wu, X. Wang, C. Fang, Y. Wang, X. Liu, Constructing amorphous RuxOy on CuO/Cu2O nanowire arrays for improved oxygen evolution, J. Nanopart. Res. 22 (2020) 125, https://doi.org/10.1007/s11051-020-04859-x.
[120] F. Bayat, S. Sheibani, Enhancement of photocatalytic activity of CuO-Cu2O heterostructures through the controlled content of Cu2O, Mater. Res. Bull. 145 (2022) 111561, https://doi.org/10.1016/j.materresbull.2021.111561.
[121] J. Sanetuntikul, C. Chuaicham, Y.-W. Choi, S. Shanmugam, Investigation of hollow nitrogen-doped carbon spheres as non-precious Fe–N $_4$ based oxygen reduction catalysts, J. Mater. Chem. A 3 (2015) 15473–15481, https://doi.org/10.1039/C5TA02677F.
[122] CO2 activation on Cu/TiO2 nanostructures: importance of dual binding site, e202300757, Chem. Eur. J. 29 (2023) e202300757, https://doi.org/10.1002/chem.202300757.
[123] C. Chen, X. Yan, Y. Wu, S. Liu, X. Sun, Q. Zhu, R. Feng, T. Wu, Q. Qian, H. Liu, L. Zheng, J. Zhang, B. Han, The *in situ* study of surface species and structures of oxide-derived copper catalysts for electrochemical CO $_2$ reduction, Chem. Sci. 12 (2021) 5938–5943, https://doi.org/10.1039/D1SC00042J.
[124] W. Luo, X. Nie, M.J. Janik, A. Asthagiri, Facet dependence of CO2 reduction paths on Cu electrodes, ACS Catal. 6 (2016) 219–229, https://doi.org/10.1021/acscatal.5b01967.
[125] A. Loiudice, P. Lobaccaro, E.A. Kamali, T. Thao, B.H. Huang, J.W. Ager, R. Buonsanti, Tailoring copper nanocrystals towards C2 products in electrochemical CO2 reduction, Angew. Chem. Int. Ed. 55 (2016) 5789–5792, https://doi.org/10.1002/anie.201601582.
[126] A.H.M. da Silva, S.J. Raaijman, C.S. Santana, J.M. Assaf, J.F. Gomes, M.T. M. Koper, Electrocatalytic CO2 reduction to C2+ products on Cu and CuxZny electrodes: Effects of chemical composition and surface morphology, J. Electroanal. Chem. 880 (2021) 114750, https://doi.org/10.1016/j.jelechem.2020.114750.
[127] J. He, T. Dou, S. Diao, Y. Wang, X. Zhao, F. Zhang, X. Lei, Cu/Fe $_3$ O $_4$ nanocomposites from layered double hydroxides as catalysts for selective electroreduction of carbon dioxide, ACS Appl. Nano Mater. 6 (2023) 13543–13550, https://doi.org/10.1021/acsanm.3c02193.
[128] J.H. Lee, W. Jang, H. Lee, D. Oh, W.Y. Noh, K.Y. Kim, J. Kim, H. Kim, K. An, M. G. Kim, Y. Kwon, J.S. Lee, S. Cho, Tuning CuMgAl-layered double hydroxide nanostructures to achieve $CH_4$ and $C_{2+}$ product selectivity in $CO_2$ electroreduction, Nano Lett. 24 (2024) 9322–9330, https://doi.org/10.1021/acs.nanolett.4c02233.
[129] Y. Gao, Z. Zhang, J. Wu, X. Yi, A. Zheng, A. Umar, D. O'Hare, Q. Wang, Comprehensive investigation of CO2 adsorption on Mg–Al–CO3 LDH-derived mixed metal oxides, J. Mater. Chem. A 1 (2013) 12782, https://doi.org/10.1039/c3ta13039h.
[130] S. Ishihara, P. Sahoo, K. Deguchi, S. Ohki, M. Tansho, T. Shimizu, J. Labuta, J. P. Hill, K. Ariga, K. Watanabe, Y. Yamauchi, S. Suehara, N. Iyi, Dynamic breathing of CO2 by hydrotalcite, J. Am. Chem. Soc. 135 (2013) 18040–18043, https://doi.org/10.1021/ja4099752.
[131] J. Hong, W. Zhang, Y. Wang, T. Zhou, R. Xu, Photocatalytic reduction of carbon dioxide over self-assembled carbon nitride and layered double hydroxide: the role of carbon dioxide enrichment, ChemCatChem 6 (2014) 2315–2321, https://doi.org/10.1002/cctc.201402195.
[132] G. Gurudayal, J.W. Beeman, J. Bullock, H. Wang, J. Eichhorn, C. Towle, A. Javey, F.M. Toma, N. Mathews, J.W. Ager, Si photocathode with Ag-supported dendritic Cu catalyst for $CO_2$ reduction, Energy Environ. Sci. 12 (2019) 1068–1077, https://doi.org/10.1039/C8EE03547D.